UNIVERSITY OF TWENTE.

Faculty of Engineering Technology.

INTEGRAL BOUNDARY LAYER PARAMETERS

AERODYNAMICS DIVISION OF SUZLON BLADE TECHNOLOGY

Joel Matos s1815822

ME-TFE

Prof.Dr.Ir. C.H. Venner

Prof.Dr.Ir. H.W.M. Hoeijmakers

Eng. Sonia Salcedo

Preface

This document comprises the results and conclusions that follow the internship at the Aerodynamics Division of Suzlon Blade Technology Hengelo as a part of the Master's program in Mechanical Engineering at the Faculty of Engineering Technology, University of Twente. A note of appreciation is left here to the A&L Department team for providing this opportunity and the assistance throughout the project.

Table of Contents

List of Figures

List of Tables

Nomenclature

c	:	Airfoil chord
c_d	:	Drag coefficient
c_p	:	Pressure coefficient
c_f	:	Skin Friction coefficient
Re	:	Reynold's number
U_e	:	Boundary layer velocity
δ	:	Boundary layer thickness
δ_1	:	Displacement thickness
δ_2	:	Momentum thickness
α	:	Angle of attack
SS	:	Suction Side
PS	:	Pressure Side

Abstract

The integral boundary layer parameters and the shape of the velocity profile at the trailing edge are determinant parameters in the characterization of the aero acoustical performance of an airfoil. Despite the development in numerical solvers some unclear definitions still lead to incoherencies between different numerical and experimental results. Namely, defining the chord percentage position at which the velocity profile should be analyzed and how to determine the boundary layer thickness are two uncertainties. Chord percentage is usually in the close vicinity of one, either before or after. The problem of determining the boundary layer thickness at the trailing edge arises from the fact that the flow around the airfoil is not a non-pressure gradient flow field. Thus, the traditional definition considering the point at which the velocity is ninety nine percent of the freestream velocity will produce inconsistent results. In this assignment post process tools are developed to deal with such calculations for subsonic flows around airfoils considering these particularities. Using an in-house standardized numerical simulation procedure several case studies with different airfoils and conditions are computed. Some cases are used to determine the competence of the developed tools and others to evaluate the correctness of the numerically generated results by benchmarking them against results from other CFD simulations, experimental setups, and Xfoil.

1 Introduction

Wind energy is a source of renewable power that uses the energy in air currents flowing across the surface of planet earth. Wind turbines harvest this kinetic energy and convert it into usable power. Electricity generating wind turbines employ proven and tested technology and provide a secure and sustainable energy supply. Wind is an unlimited and free renewable resource, a natural occurrence, and harvesting the kinetic energy of wind doesn't affect currents or wind cycles in any way. Harvesting wind power is a clean, non-polluting way to generate electricity. Unlike other types of power plants, it emits no air pollutants or greenhouse gases. Wind turbine blades convert the energy of the wind into usable shaft power called torque. Energy is extracted from the wind by decelerating the flow as it passes over the blades. The forces which decelerate the wind are equal and opposite to the thrust type lifting forces that rotate the blades. The lift forces are generated due to the geometry of the blades that create a low pressure (suction) and high pressure (pressure) side. The net result is a lifting force perpendicular to the direction of flow of the air over the turbines blade. The amount of power transferred is dependent on the rotor size and the wind speed, wind turbines can generate from 100 kilowatts up to several megawatts. Larger wind turbines are more cost effective and are grouped together into wind farms, which provide bulk power to the electrical grid. Offshore wind turbines are larger and can generate more power. If the turbine blades rotate too slowly, a bigger portion of the flow passes undisturbed and not as much energy is extracted from the wind currents as it potentially could. On the other hand, if the blades rotate too quickly, it appears to the wind as a large flat rotating disc creating more drag. Then the optimal tip speed ratio, TSR, which is defined as the ratio of the speed of the rotor tip to the wind speed, depends on the rotor blade length and the wind turbine blade design itself. For these reasons, determining the flow field around the blades its essential to study the phenomena that define the blade performance. The flow field can be determined through direct numerical simulations DNS, large eddy simulations (LES) or Reynolds Averaged Navier-Stokes (RANS) methods. Due to the large computational cost, DNS and LES are currently not practical for realistic Reynolds numbers. Thus, for design purposes RANS methods are used. In RANS several assumptions are considered in the models used to solve boundary layers, turbulence, transition, and other phenomena. Suitable models are crucial for an accurate prediction of the flow field characteristic and consequently the aerodynamics and aeroacoustical performance of the wind turbine blades. A set of tools is developed to evaluate the quality of the numerical simulations and how some of assumptions and considerations are reflected in the solution obtained.

2 Reference Background

In the BPM report [1] an overall prediction method has been developed for the self-generated noise of an airfoil blade encountering smooth flow. Prediction methods for individual self-noise mechanisms are semi-empirical and are based on previous theoretical studies and the most comprehensive self-noise data set available. The specially processed data set, most of which is newly presented in this report, is from a series of aerodynamic and acoustic tests of two- and three-dimensional airfoil blade sections conducted in an anechoic wind tunnel. The data base, with which the predictions are matched, is from seven NACA 0012 airfoil blade sections of different sizes (chord lengths from 2.5 to 61 cm) tested at wind tunnel speeds up to Mach 0.21 (Reynolds number based on chord up to 3 x 106) and at angles of attack from 0 ° to 25.2 °. The predictions are compared successfully with published data from three self-noise studies of different airfoil shapes, which were tested up to Mach and Reynolds numbers of 0.5 and 4.6 x 106, respectively. The objective of the BANC-II workshop [2] was to assess the present computational capability in physics-based prediction of different types of airframe noise problems and to advance the state-of-the-art via a combined effort. This paper summarizes the results from the prediction of broadband turbulent boundary-layer trailing-edge noise and related source quantities. 2D airfoil sections, namely a NACA0012 and DU-96-180, served as test cases. Code-to-code comparisons in this category were mainly restricted to relatively fast RANS-based methods applying statistical noise theory. Overall, the prediction capability was sufficient to capture the principal trailing-edge far-field noise scaling behavior in the mid-frequency range i.e. the measured dependence of noise on angle-of-attack or free stream velocity. Differences in predicted trends appeared at lower and higher frequencies. Moreover, a comparatively large scatter among the DU-96-180 prediction results was observable, indicating individual room for improvement in the applied approaches. The BANC-III workshop [3] documentation summarizes the results from the prediction of broadband turbulent boundary-layer trailing-edge noise and related source quantities. Since the forerunner BANC-II workshop identified some room for improvements in the achieved prediction quality, BANC-III relies on the same test cases, namely 2D NACA0012 and DU96-W-180 airfoil sections in a uniform flow. Compared to BANC-II particularly the scatter among predictions for the DU96-W-180 test case could be significantly reduced. However, proposed adaptations of previously applied computational methods did not systematically improve the prediction quality for all requested parameters.

Noise predictions require the determination of the flow field, thus in the documents mentioned above data regarding the integral boundary layer parameters and the normal velocity profile at certain positions of the airfoil is available for comparison.

3 Internship: Integral Boundary Layer Parameters

3.1 Task

The purpose of this work is to generate and verify post process tools that calculate integral boundary layer parameters using flow field data from RANS simulations.

3.1.1 Description

Characterizing the phenomena occurring in the boundary layer is crucial when predicting the aerodynamical and aeroacoustical performance of the airfoil. The script is used in multiple cases with different airfoils and flow field conditions. The results obtained are compared to data from Xfoil and several scientific papers compiling numerical and experimental results. The post process tools are developed in Python. For some of the case studies a general agreement has been reached regarding the results and these are used as a benchmark, giving insight on the correctness of the generated post process tools. The scripts are then verified and used to validate the results obtained through the RANS simulations.

As mentioned above, the developed script handles different airfoils and conditions. Consequently, besides the flow field solution from the simulation, the airfoil geometry is also an input. Although most of the attention will be drawn towards the trailing edge, it is possible to calculate the integral boundary layer parameters throughout the whole surface of the airfoil. The program comprises functions that load the information from the simulations and the airfoil geometry, calculate the normal vector to a point on the surface, interpolate the normal velocity profile, and calculate the required parameters. The correspondent data flow diagram is presented in (**Fig. 1**).

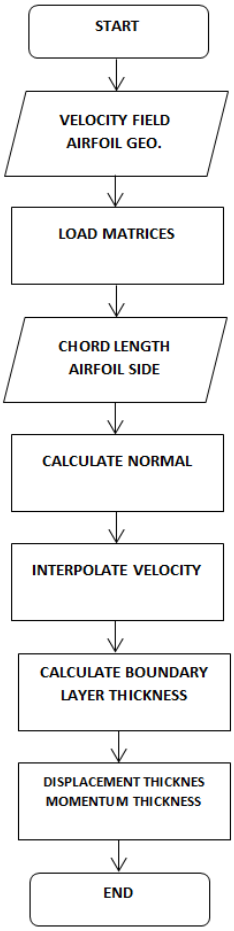

Fig. 1: *Script Data Flow Chart*

In (**Fig. 1**) the second level "Load Matrices" corresponds to the function that converts the ASCII input files into matrices. The input at the third level locates the pretended point on the surface of the airfoil since the chord length percentage and airfoil side (Suction or Pressure) are prescribed. At the fourth level the normal direction to the airfoil surface pointing outwards is calculated and points along this same direction are generated. The velocity vector is interpolated at the points generated along the normal direction. Next, the boundary layer thickness is calculated according to [2] and is used to determine the remaining parameters at the last level as in [4].

3.1.2 Methodology

1. Self-Similarity is analyzed.
2. Comparison of the Cp and Cf distributions.
3. Comparison of the integral boundary layer parameters at the trailing edge.
4. Comparison of the velocity profile at the trailing edge (if available)

The cases considered involve the study of five different airfoils: UL Airfoil, NACA0012, LL Airfoil, HL Airfoil, and CL Airfoil. The UL Airfoil case study is used to validate the scripts because the standerdized numerical simulations for this case had previously been analyzed and approved, the remaining airfoils are used to evaluate the performance of the in-house standardized numerical simulation procedure for each case, and how parameters like the mesh density and laminar-turbulent transition affect the computations. The velocity profile self similarity is verified, differences between the Cp and Cf of different numerical and experimental setups, the velocity profile at the trailing edge is compared with other CFD and experimental results (if available), and the calculated integral boundary layer parameters are measured against results from Xfoil, CFD and experiments. The first two points are used to check the correctness of the obtained profiles, according to [4], before proceeding to calculate and compare the remaining parameters.

3.1.3 Timeline

The internship is carried for twelve weeks. The specific aims and timelines for this assignment are presented below

		November				December				January			
	Week	1	2	3	4	5	6	7	8	9	10	11	12
Chore	Literature Study												
	Software Learning												
	Script Development												
	Selection Of The Case Studies												
	Data Compilement and Report												

Table 1: *Internship Timeline*

3.2 Results

3.2.1 UL Airfoil

In [3] the same airfoil and angle of attack were used with a similar Reynolds Number; thus, it is possible to benchmark the results obtained against other CFD simulations. The conditions considered for these simulations are given in table 2.

	Calculated Results	DTU	IAG	DLR
Chord Length l_c (m)	1	0.4	0.4	0.4
B.L. Fixed Transition Position x_c/l_c	SS= Fully Turbulent PS= Fully Turbulent	SS= 0.12 PS=0.67	SS= 0.12 PS= 0.15	SS= 0.12 PS= 0.15
Reynolds Number	$1.3*10^6$	$1.13*10^6$	$1.13*10^6$	$1.13*10^6$

Table 2: *Simulation parameters for the UL Airfoil*

The profile similarity is verified for the velocity field obtained in the simulation. From (**Fig. 2**) it is concluded that there is an overall agreement of the pressure coefficient distributions for the DLR, IAG, DTU, and Calculated Results case studies. The IAG results show only a 5 percent offset at the leading edge on the pressure side.

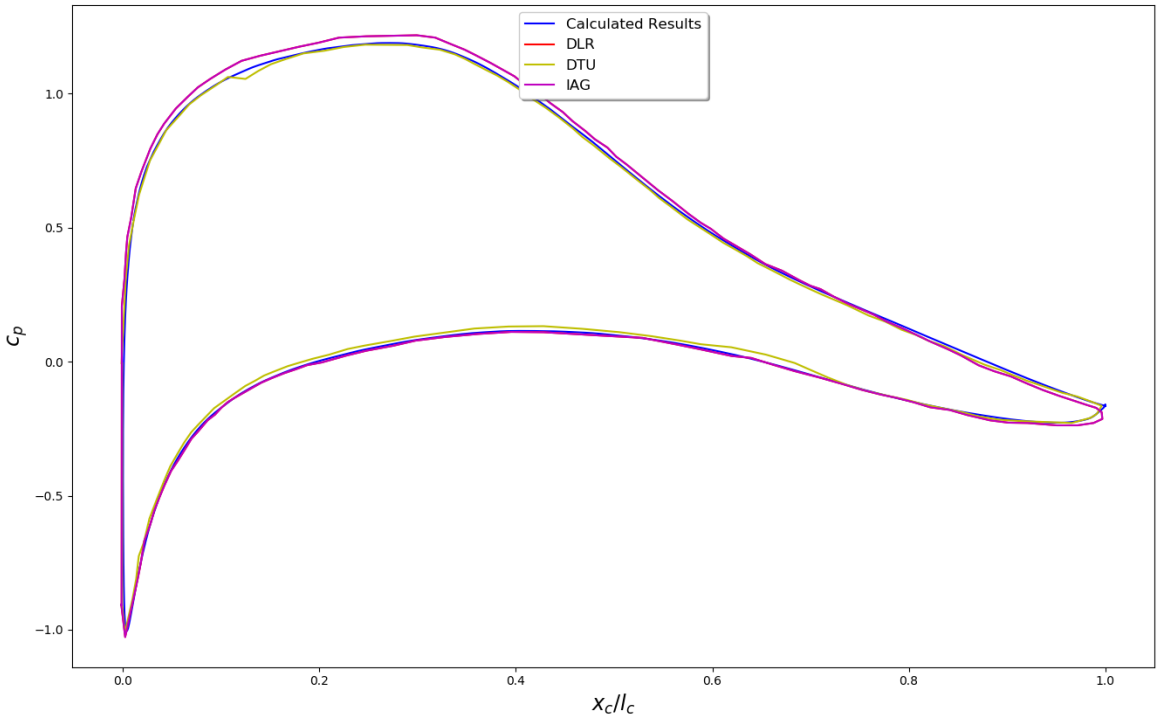

Fig. 2: *Pressure coefficient distribution considering free transition UL*

The plots for the different skin friction c_f distributions are presented in (**Fig. 3**). The plots are as expected: noticeably different at the leading edge due to the fact that the Calculated Results consider a fully turbulent boundary layer whereas the other simulations deal with tripped profiles and the distributions assume similar values closer to the trailing edge .For the pressure side, the differences between the DTU results and the remaining simulations reflect the setting of the laminar-turbulent transition at $x_c/l_c = 0.67$.

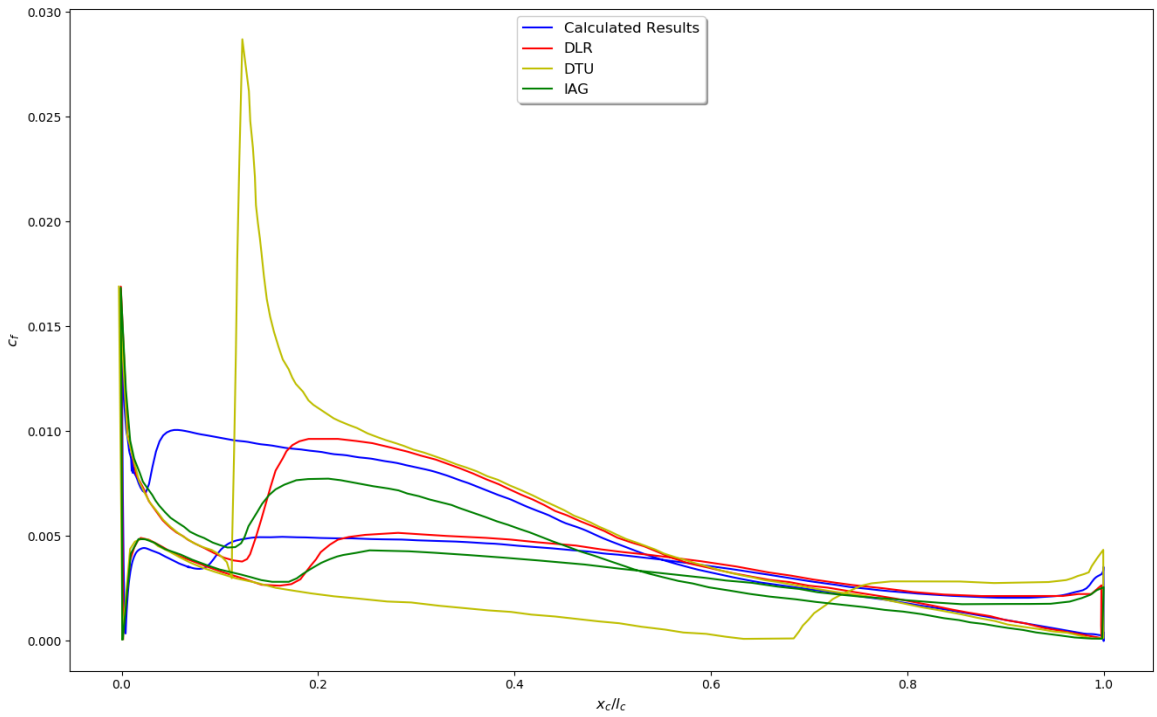

Fig. 3: *Skin Friction coefficient distribution considering free transition UL*

The velocity profiles are presented in (**Fig. 4**) and the values for the different boundary layer integral parameters are presented in table 3.

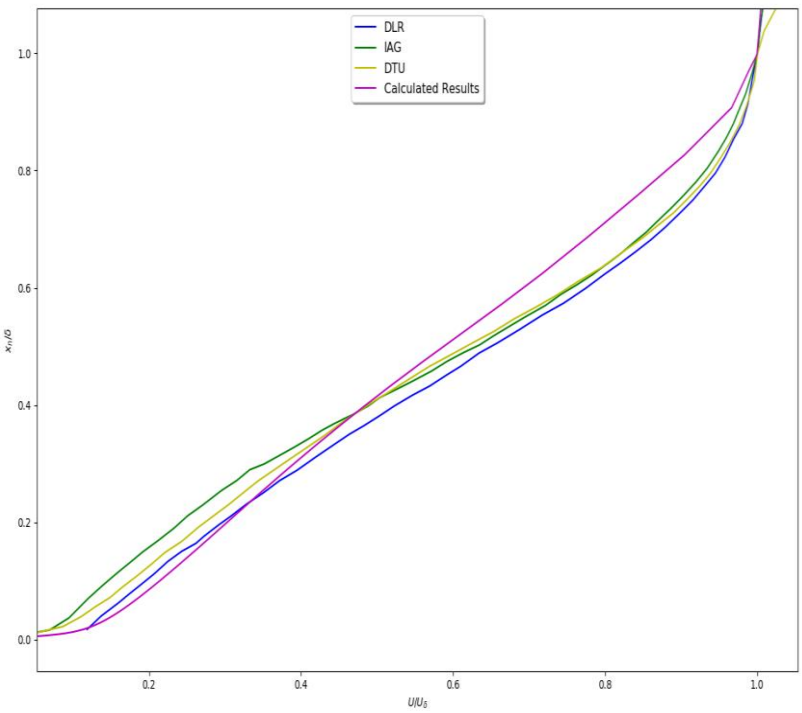

Fig. 4: *Comparison of the velocity profiles at the trailing edge*

	δ / l_c, SS	δ_1 / l_c, SS	δ_2 / l_c , SS
Calculated Results	39.90	16.58	6.73
DLR	41.20	16.67	6.67
IAG	42.60	20.33	8.00
DTU	41.90	18.86	7.33

Table 3: *Integral boundary layer parameters values at the trailing edge for the UL Airfoil*

The DLR simulations computed the closest values to the ones obtained in Calculated Results having a difference of 3.16, 1.74, and 0.89 percent for the boundary layer thickness, displacement thickness, and momentum thickness, respectively. In the IAG results the biggest discrepancy relatively to the Calculated Results is a value of 18.45 percent for the displacement thickness and for the boundary layer and momentum thickness differences of 6.33 and 15.87 are verified. The offset between the values calculated in the DTU and the Calculated Results case studies for the boundary layer, displacement, and momentum thickness are 4.77, 12.09, and 8.18 percent.

3.2.2 NACA 0012

The conditions for the first case study are presented in **Table 4**.

	NACA 0012
Chord Length l_c (m)	1
B.L. Fixed Transition Position x_c/l_c (SS: Suction Side PS: Pressure Side)	SS= Fully Turbulent PS= Fully Turbulent
Re	$1.5*10^6$
α	0,4,6

***Table 4**: Simulation parameters for the first case studies.*

The first step is to check for profile similarity in the fully turbulent region. Before comparing the profiles at different locations, it is necessary to non-dimensionalize the data. The characteristic scales used to non-dimensionalize the normal distance to the airfoil surface and the velocity at the different points are the boundary layer thickness δ and the velocity at the limit of the boundary layer U_δ. In this case, the velocity profiles at $x_c/l_c = 0.6$ and $x_c/l_c = 0.80$ are juxtaposed to check for profile similarity.

<u>Angle Of Attack 4º:</u>

The plot for the suction side are presented in (**Fig. 5**) whereas (**Fig. 6**) corresponds to the pressure side of the airfoil. It is concluded from (**Fig. 5**) that the overall shape of the profile is similar with a slight offset between the two plots around the region comprehended between 0.6 and 1 along the horizontal axis.

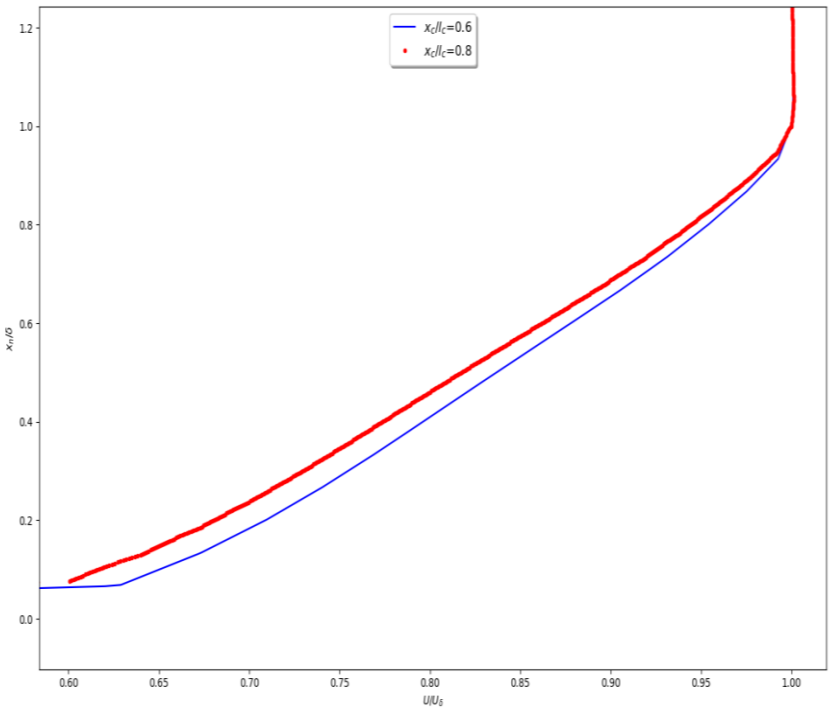

***Fig. 5**: Suction Side Velocity Profile Comparison*

In (**Fig. 6**) presented below, similar results were obtained for the pressure side regarding the shape and differences of the profiles.

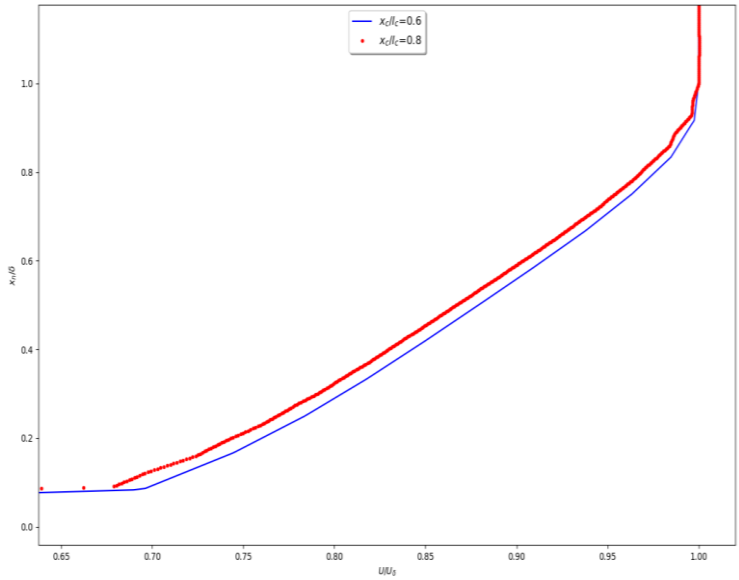

***Fig. 6**: Pressure Side Velocity Profile Comparison*

Although the profiles do not match in their entirety, the general agreement between the shapes suggests that the differences do not refute the correctness of the results.

The same airfoil, Reynolds number, and angle of attack were used in [2], thus it is possible to benchmark the results obtained against other CFD simulations. In this document, data for the pressure coefficient, skin coefficient, velocity profiles, and boundary layer integral parameters is available from different institutions. The conditions considered for these simulations in [2] are given in table 5. Experimental data for the velocity profile and pressure coefficient is also provided.

	UoA	IAG	DLR
Chord Length l_c (m)	0.4	0.4	0.4
B.L. Fixed Transition Position x_c/l_c (SS: Suction Side PS: Pressure Side)	SS= Fully Turbulent PS= Fully Turbulent	SS= 0.065 PS= 0.065	SS= 0.065 PS= 0.065
Reynolds Number	$1.5*10^6$	$1.5*10^6$	$1.5*10^6$

***Table 5:** Simulation parameters in [2] for α=4º*

From (**Fig. 7**) it is concluded that there is an overall agreement of the pressure coefficient distributions for the DLR, IAG, and Calculated Results case studies. The experimental results show only a slight offset on the region close to the pressure side peak when compared to the previously mentioned cases. However, the UoA c_p distribution exhibits differences relatively to the other case studies on both sides of the airfoil: close to the suction side peak and throughout the whole pressure side.

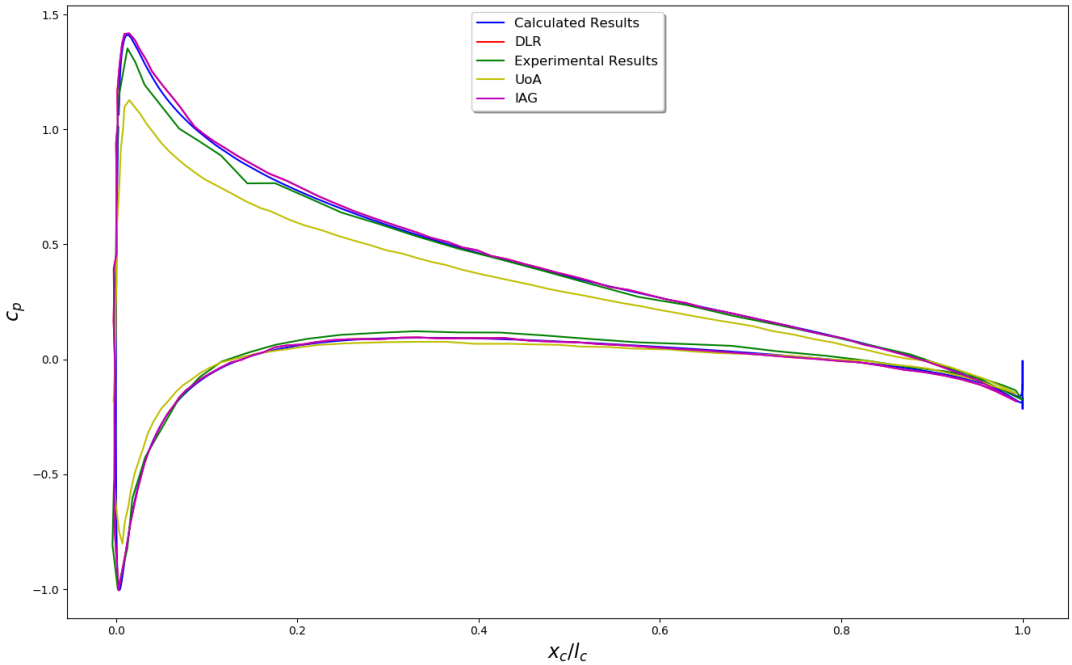

Fig. 7: *Pressure coefficient distribution for α=4°*

The plots of the skin friction coefficient c_f for the suction and pressure side of the airfoil are presented in (**Fig. 8**) and (**Fig. 9**), respectively. In both plots, the first peak on each c_f distribution corresponds to the point of maximum velocity, for the Calculated Results the peak is not as elevated as the remaining cases.

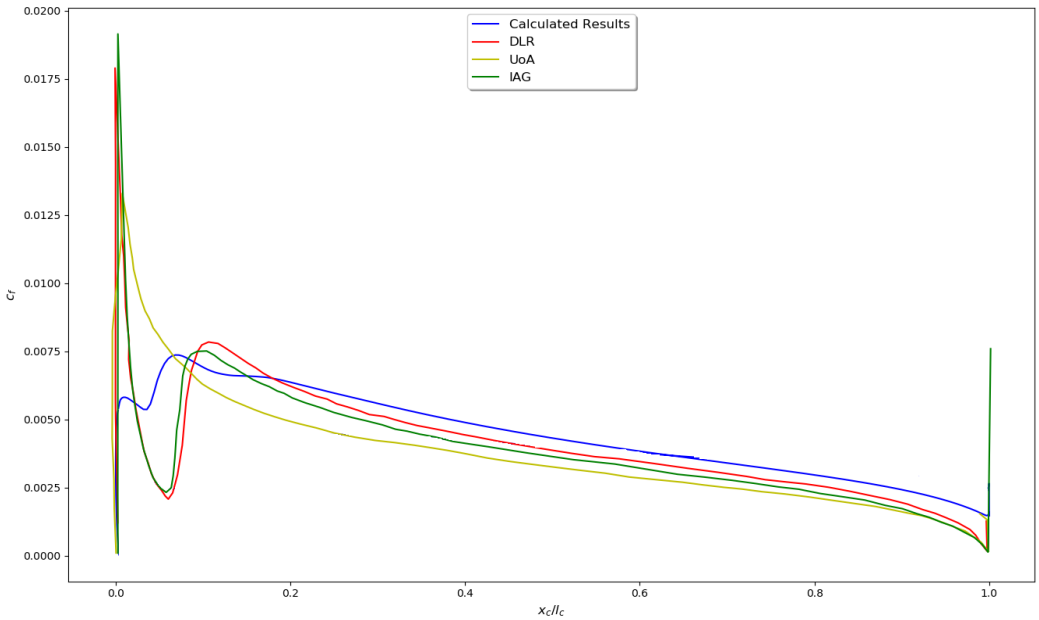

Fig. 8: *Skin friction coefficient distribution for α=4° at the suction side*

Concerning the suction side, the depression for the DLR and IAG cases corresponds to the tripping of the flow, for the Calculated Results it is a consequence of the method used to solve the boundary layer (no tripping is considered in this case), and for UoA no depression is present because this simulation considers a fully turbulent velocity profile.

The arguments used to justify the shape of the skin friction coefficient distributions on the suction side explain the plots in (Fig. 9) for the pressure side of the airfoil.

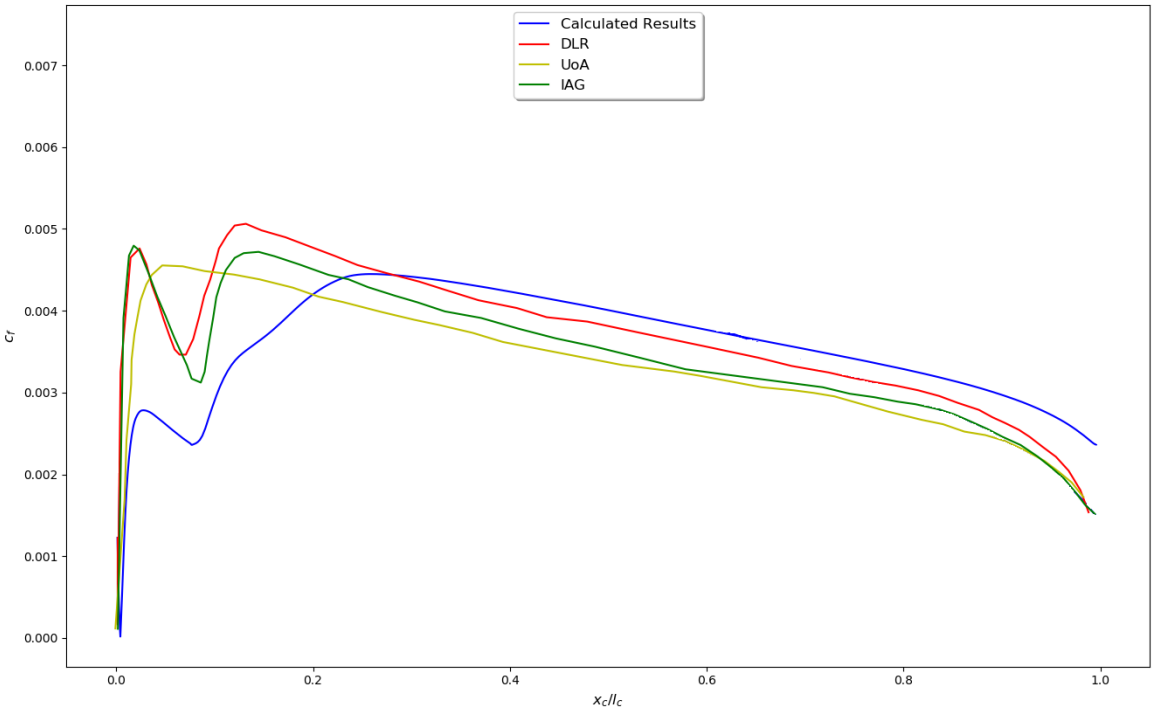

Fig. 9: *Skin friction coefficient distribution for α=4° at the pressure side*

Congruent pressure and skin friction coefficient distributions is a necessary but not sufficient condition to obtain similar results for different simulations/experiments as far as velocity profiles and integral boundary layer parameters are concerned. The different velocity profiles are presented in (**Fig. 10**).

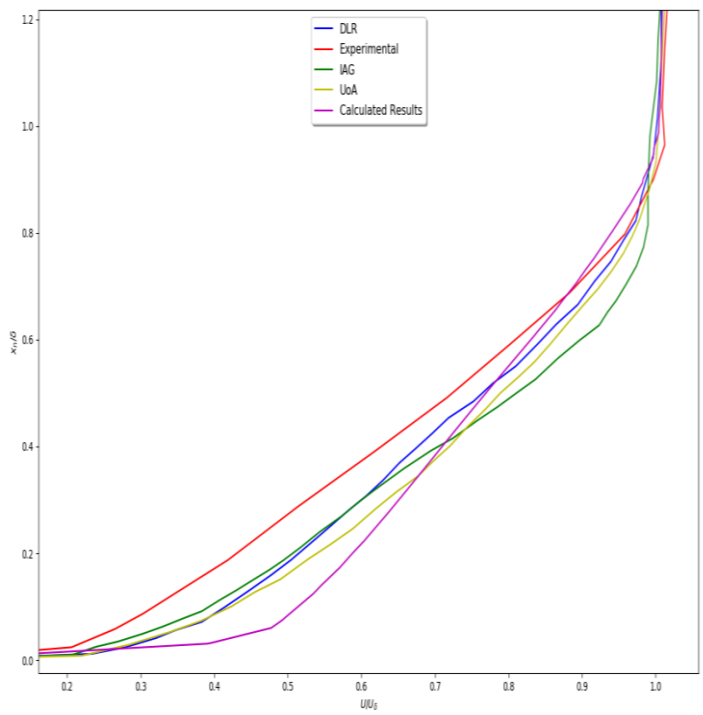

Fig. 10: *Trailing edge velocity profiles for α=4° at the suction side*

Although the boundary layer thickness at the trailing was captured correctly, the velocity profile shape itself differs from the shapes obtained in the other cases. In the Calculated Results numerical simulations, the values of y+ were in the range between 100 and 300 which means that wall functions were used to solve the boundary layer.

The dimensionless integral boundary layer parameters are summarized in Table 6. Compared to the Experimental Results, the Calculated Results underestimated the three parameters having a difference of 22.83, 35.10, and 22.64 percent for the boundary layer thickness, displacement thickness, and momentum thickness, respectively. This contrast can be explained by the incongruity between the shape of the two velocity profiles. The same conclusions are drawn when comparing the Calculated Results with the DLR, IAG, and UoA case studies, although the differences are smaller. Regarding Xfoil the values for the momentum and displacement thickness vary by less than 1 percent whereas the boundary layer thickness differs by 14 percent. The comparisons with the BPM results show similar differences to the Experimental Results case study, this coincidence was expected since the boundary layer parameters equations in BPM were obtained by fitting curves to match experimental data [1].

It is also concluded from the table that the values obtained by DLR, IAG, and UoA for the parameters are closer to the Experimental Results. However, the results computed by the referenced institutions also tend to underestimate the integral boundary layer parameters. Although the c_p distribution for the UoA case study deviated the most from the Experimental Results, the parameters calculated by this institution are the closest to the experimental measurements.

	$\delta/\ l_c$, SS	$\delta_1/\ l_c$, SS	$\delta_2/\ l_c$, SS
Calculated Results	27.78	7.78	4.45
Experimental Results	36.00	12.00	5.75
DLR	32.50	9.25	5.00
IAG	34.50	9.00	4.50
UoA	38.75	10.00	5.75
Xfoil	32.34	7.72	4.42
BPM	-	11.42	6.08

Table 6: *Trailing edge integral boundary layer parameters for α=4°*

In [2] the data concerning the velocity profile and the relevant parameters is only available for the trailing edge. However, Xfoil calculates the boundary layer parameters throughout the whole surface of the airfoil. Thus, it is possible to make a comparison with the Calculated Results on how the values of the displacement and momentum thickness change along the airfoil. The plots for the displacement and momentum thickness are given in (**Fig. 11**) and (**Fig. 12**), respectively. For both parameters, the evolution throughout the airfoil for Xfoil and Calculated Results follows the same trend. Additionally, the values of the parameters are similar for the two studies, except at the leading edge. The discrepancy at the leading edge is related to the fact that Xfoil considers a velocity field tripped at $x_c/l_c = 0.065$ whereas a fully turbulent profile was assumed in the Calculated Results simulations.

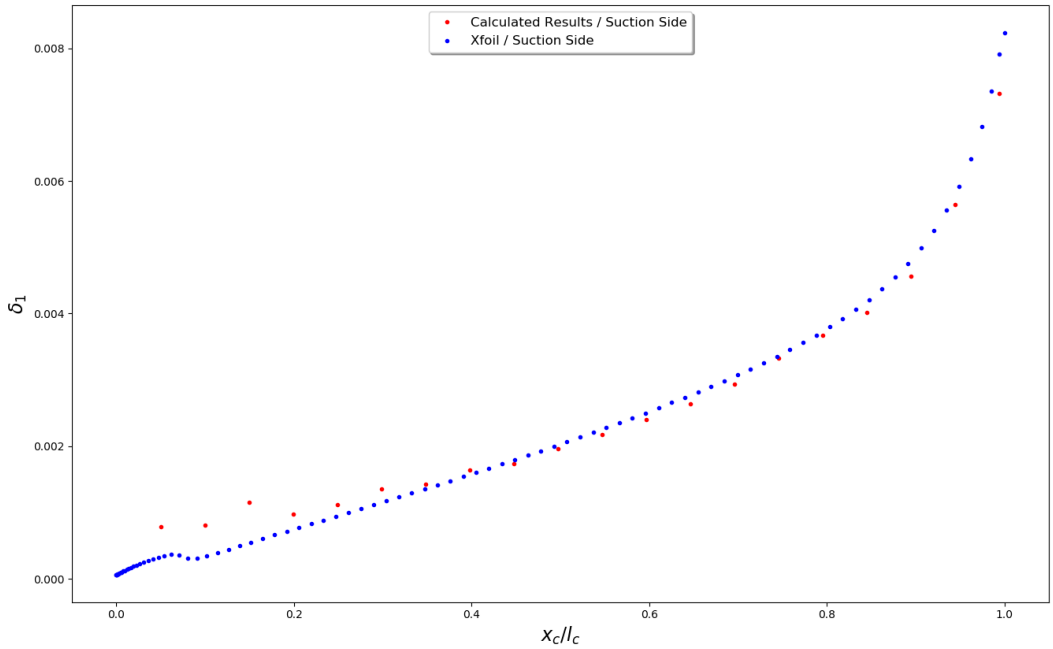

Fig. 11: *Displacement thickness evolution throughout the suction side of the airfoil*

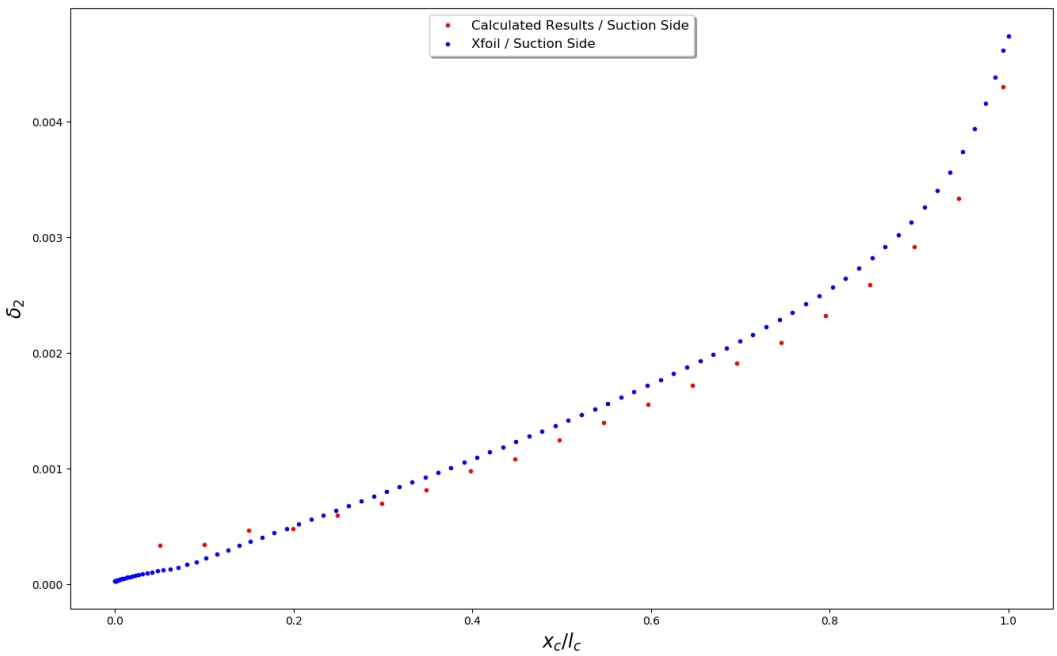

Fig. 12: *Momentum thickness evolution throughout the suction side of the airfoil*

The angle of attack α influences the complexity of the flow field around the airfoil. Thus, it is of interest to determine how the integral boundary layer parameters change with the variation of the α parameter and whether the CFD results error relatively to the experimental results is dependent on the angle of attack. The CFD and experimental results in [2] are again used as benchmarks for the Calculate Results. Two other angles of attack are considered α=0° and α=6°, while the rest of the parameters are the same as in table 5. The results obtained for the different integral boundary layer parameters are summarized in tables 7 and 8 for a zero and six degrees angle of attack, respectively.

	$\delta/\ l_c$, SS	$\delta_1/\ l_c$, SS	$\delta_2/\ l_c$, SS
Calculated Results	23.30	5.42	3.35
Experimental Results	31.13	7.50	4.25
DLR	30.25	6.50	3.75
IAG	27.75	6.25	3.50
UoA	30.00	6.75	4.25

Table 7: *Trailing edge integral boundary layer parameters for α=0°*

	$\delta/\ l_c$, SS	$\delta_1/\ l_c$, SS	$\delta_2/\ l_c$, SS
Calculated Results	31.00	9.32	5.08
Experimental Results	41.25	14.25	6.25
DLR	35.00	10.75	5.50
IAG	42.50	11.00	5.25
UoA	45.00	12.75	7.00

Table 8: *Trailing edge integral boundary layer parameters for α=6°*

The results for α=4° were presented in table 6. It is concluded from the experimental data in the tables that increasing the angle of attack α results in an increase of all the integral boundary layer parameters and that the different simulations captured this trend. The error formula used to analyze the results reads:

$$e_{\%} = \left|1 - \frac{\delta_n^{CR}}{\delta_n^{EP}}\right| * 100 \qquad (1)$$

The error of the Calculated Results relative to the Experimental Results for the three angles of attack is presented in table 9.

	$\delta/\ l_c$, SS	$\delta_1/\ l_c$, SS	$\delta_2/\ l_c$, SS
α=0°	25.10	27.70	21.20
α=4°	22.83	35.30	22.40
α=6°	24.80	34.60	18.70

Table 9: *Error for the different angles of attack*

From table 9 it is concluded that the prediction of the parameters by the CFD calculations depending on the angle of attack does not follow any trend for the different parameters. The values of the boundary layer thickness error for the different angles of attack were similar, for the displacement thickness the error increased from the situation α=0° to α=4° but when the angle of attack increased to α=6° the error value remained close to error when α=4°, and for the displacement thickness the error started by increasing but then went on to decrease to a value even lower than the error when α=0°.

3.2.3 LL Airfoil

Fully Turbulent:

The parameters considered for the simulation are presented in table 10.

	Low Lift Airfoil
Chord Length l_c (m)	1
B.L. Fixed Transition Position x_c/l_c (SS: Suction Side PS: Pressure Side)	SS= Fully Turbulent PS= Fully Turbulent
Reynolds Number	$1.6*10^6$
α	4

Table 10: *Simulation parameters for the LL Airfoil*

The profile similarity is verified for the velocity field obtained in the simulation. First, a comparison with Xfoil is considered. To guarantee that the aerodynamic forces (higher level aerodynamics compared to the actual integral boundary layer parameters) are captured equally for Xfoil and Calculated Results the c_f and c_p distributions are compared. The skin friction coefficient plots in (**Fig. 13**) show that for Xfoil and Calculated Results the values computed for c_f are similar.

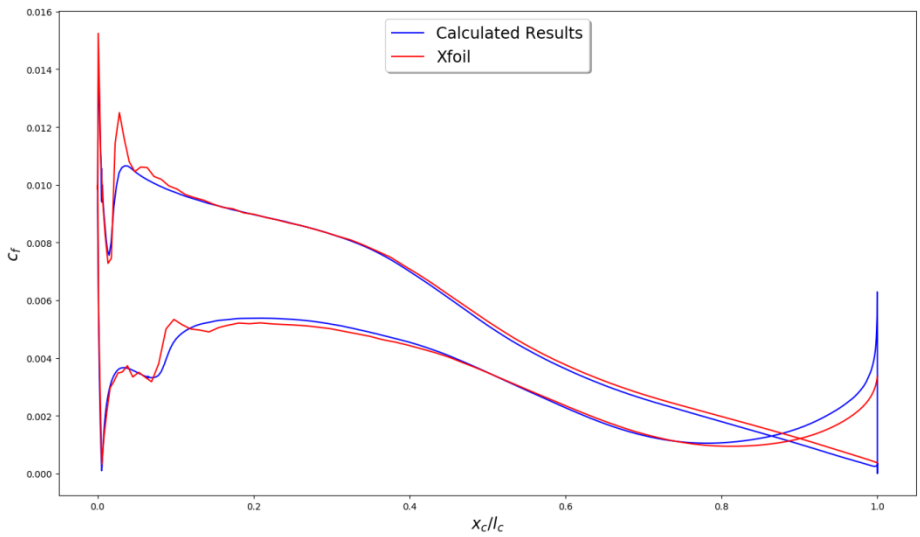

Fig. 13: *Skin friction coefficient distribution for a fully turbulent velocity field*

The pressure coefficient c_p distributions are given in (**Fig. 14**) and it is concluded that similar values are computed by Xfoil and Calculated Results. The maximum difference between the two calculations occurs at the pressure side and it is around four percent (relative to the value of c_p at that position in the Calculated Results).

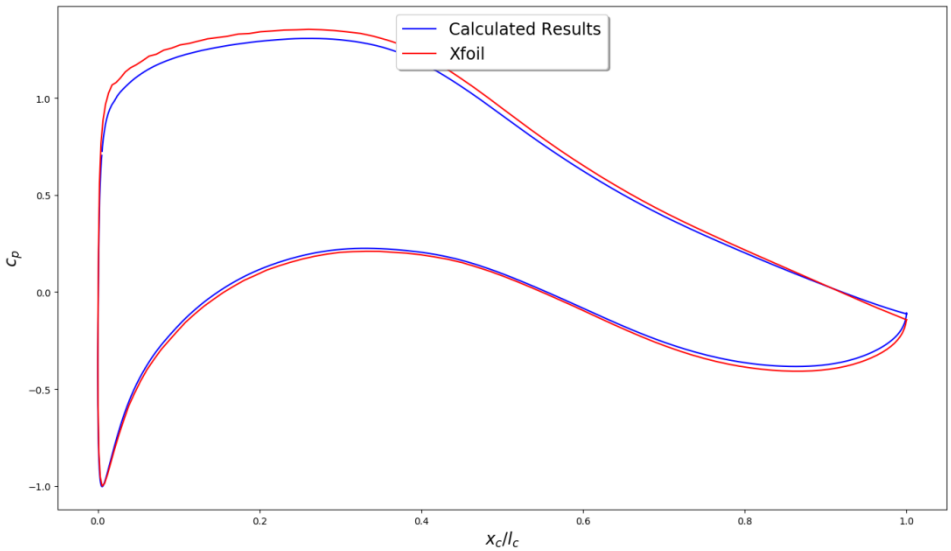

Fig. 14: *Pressure coefficient distribution for a fully turbulent velocity field*

The plots for the boundary layer integral parameters are presented in the figures below. In (**Fig. 15**) the boundary layer thickness evolution along the suction side shows that around $x_c/l_c = 0.6$ the values computed in Calculated Results start to be smaller than the results obtained from Xfoil.

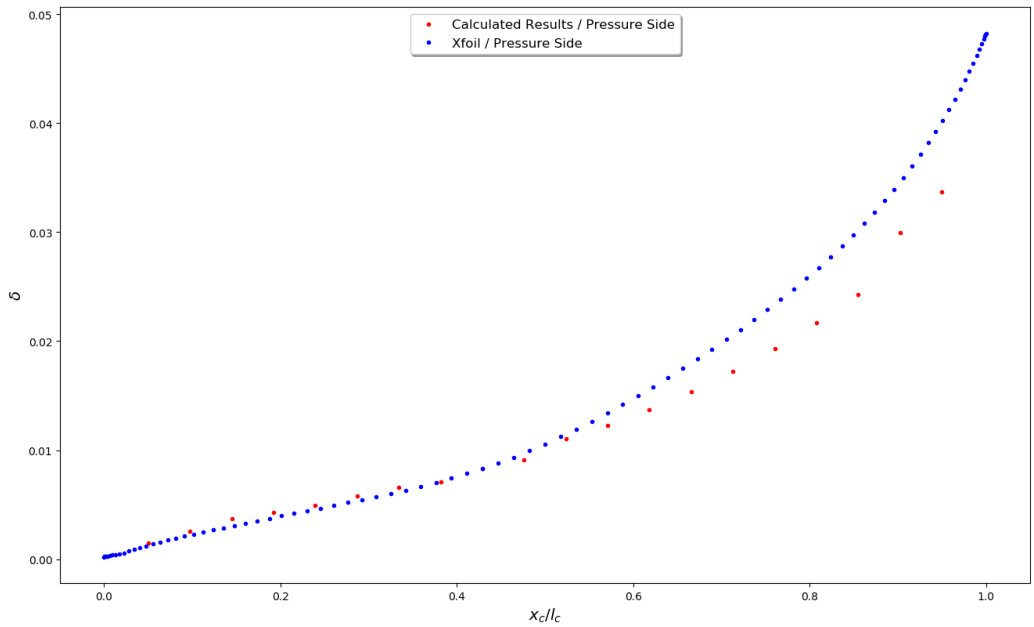

Fig. 15: *Evolution of the boundary layer thickness for a fully turbulent velocity field*

Regarding the displacement and momentum thickness, the comparisons revealed almost coincident results for the distribution of the two parameters.

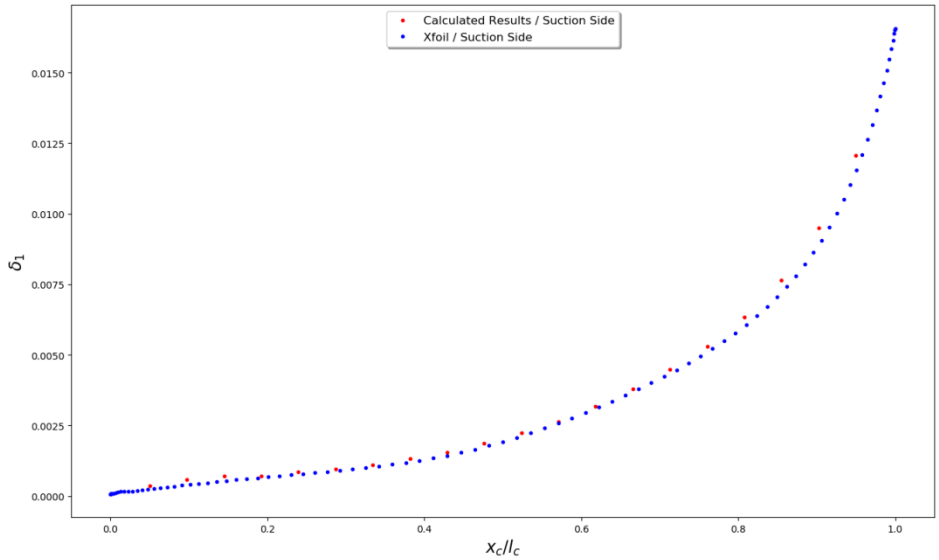

Fig. 16: *Evolution of the displacement thickness for a fully turbulent velocity field*

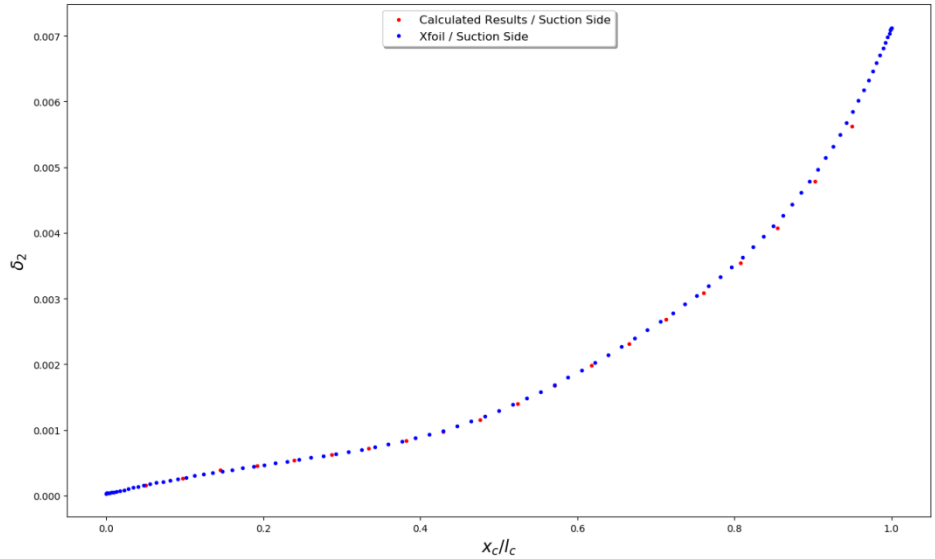

Fig. 17: *Evolution of the displacement thickness for a fully turbulent velocity field*

No boundary layer experimental data is available for the LL Airfoil. For this reason, the calculated results are compared with the NACA0012 experimental data in [2]. Although the airfoils are different, this comparison gives an idea on the correctness of the profiles obtained, specifically about the shape. The conditions for the CFD simulations and the experimental setup are summarized in table 11.

	DU93-W210	NACA0012
Chord Length l_c (m)	1	0.4
B.L. Fixed Transition Position x_c/l_c (SS: Suction Side PS: Pressure Side)	SS= Fully Turbulent PS= Fully Turbulent	SS= 0.065 PS= 0.065
Reynolds Number	$1.6*10^6$	$1.5*10^6$
α	4°	4°

Table 11: *Simulation parameters for the LL Airfoil and the NACA0012 airfoil*

The plots for the different dimensionless velocity profiles are presented in (**Fig. 18**). Compared to the Experimental Results, the Calculated Results for the LL Airfoil assume different values, but the shape of the non-dimensional profiles is similar. The shape agreement for the fully turbulent profiles is an indicator of the correctness of the velocity field computed because even though different airfoils are considered at the boundary layer level for fully developed profiles the shape agreement is expected. Contrarily to the Calculated Results numerical simulations, the values of y+ oscillated around 1 which means that wall functions were not used to solve the boundary layer.

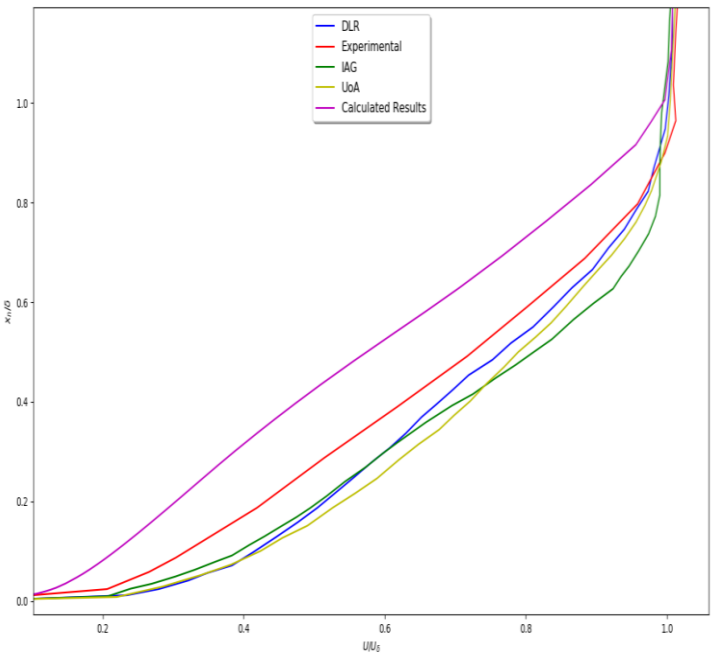

Fig. 18: *Comparing the LL Airfoil trailing edge velocity profile with the profiles for the same position in [2]*

Free Transition:

The parameters for this simulation are the same as in table 8, except the parameter regarding the location of the transition point. In this case, a natural transition velocity field along the surface of the airfoil is considered instead of a fully turbulent. The plots for the skin friction coefficient distributions are presented in (**Fig. 19**).

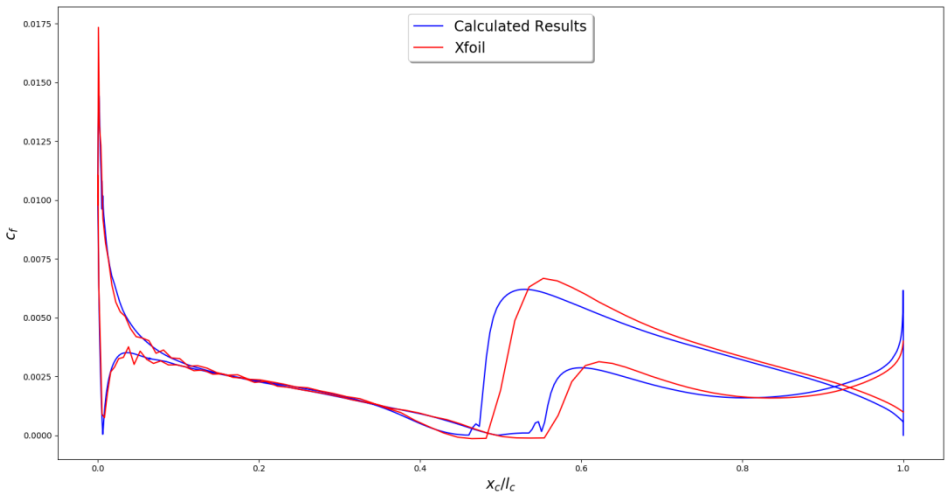

Fig. 19: *Skin friction coefficient distribution with free transition*

In (**Fig. 19**), there is and overall agreement between the two distributions, although the laminar-turbulent transition occurs at a later position for the Xfoil calculations on both sides of the airfoil, for example, on the suction side transition starts around $x_c/l_c = 0.46$ and $x_c/l_c = 0.48$ for the Calculated Results and Xfoil, respectively. The plots in (**Fig. 20**) correspond to the pressure coefficient C_p and it is concluded from the figure that the two distributions follow the same trend with a slight offset between the values of C_p itself.

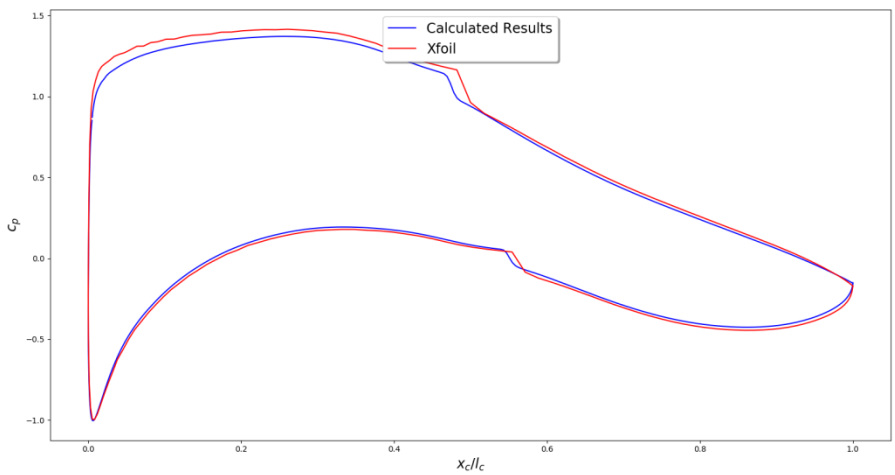

Fig. 20: *Pressure coefficient distribution with free transition*

The boundary layer thickness, displacement thickness, and momentum thickness evolutions throughout the suction side of the airfoil are presented in (**Fig. 21**), (**Fig. 22**), and (**Fig. 23**), respectively. Compared to Xfoil, the Calculated Results overestimate the boundary layer thickness before transition and underestimate it afterwards.

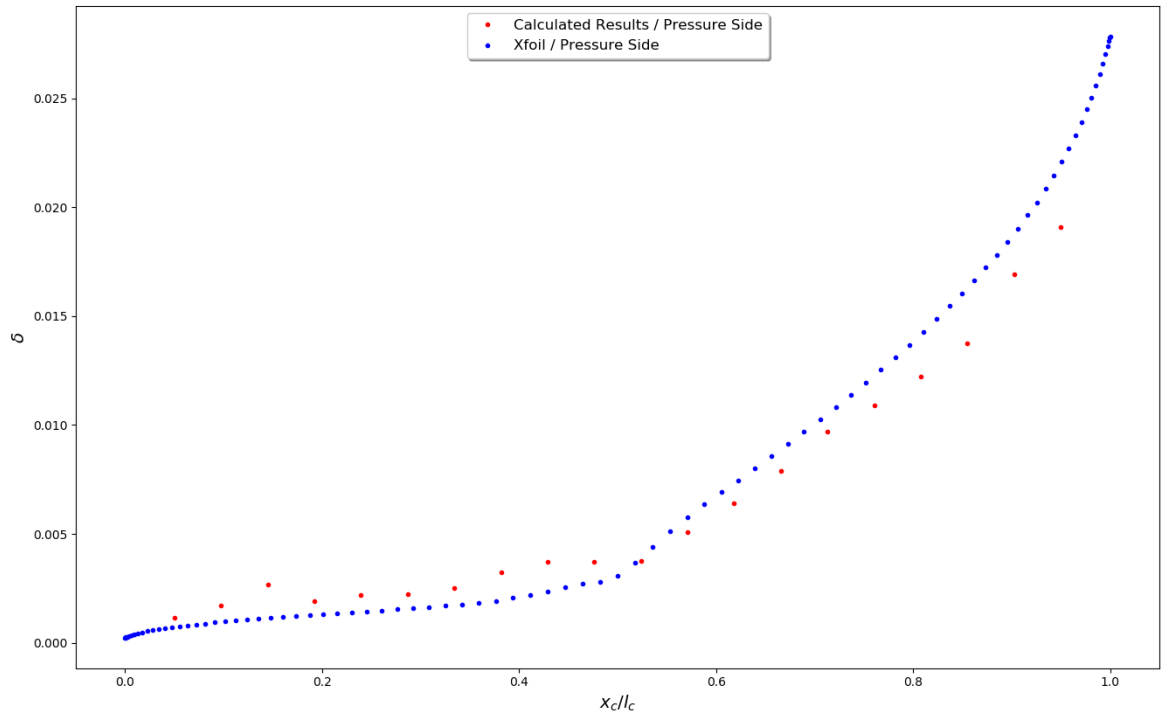

Fig. 21: *Boundary layer thickness evolution throughout the suction side of the airfoil*

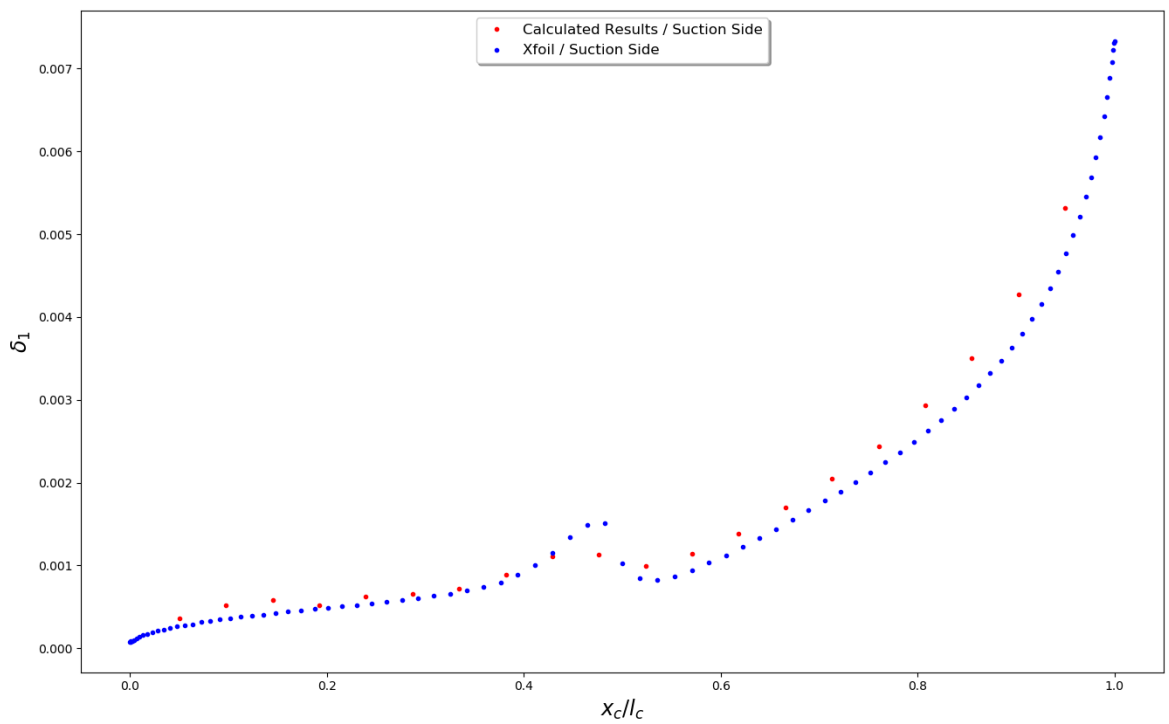

Fig. 22: *Displacement thickness evolution throughout the suction side of the airfoil*

In (**Fig. 22**) and (**Fig. 23**) the respective distributions assume similar values and the transition around $x_c/l_c = 0.47$ is captured in both calculations.

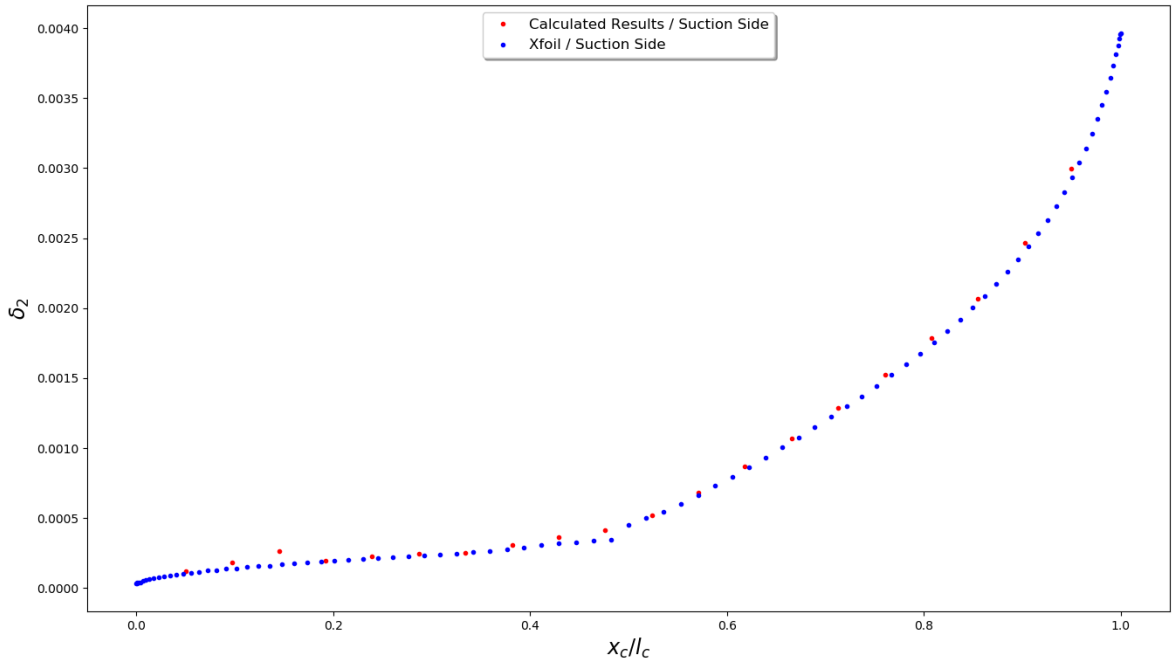

Fig. 23: *Momentum thickness evolution throughout the suction side of the airfoil*

3.2.4 HL Airfoil

Fully Turbulent:

The parameters considered for the simulation are presented in table 12.

	HL Airfoil
Chord Length l_c (m)	1
B.L. Fixed Transition Position x_c/l_c (SS: Suction Side PS: Pressure Side)	SS= Fully Turbulent PS= Fully Turbulent
Re	$3.0*10^6$
α	4

Table 12: *Simulation parameters for the HL Airfoil*

The profile similarity is verified for the velocity field obtained in the simulation. The results are benchmarked against Xfoil. The skin friction coefficient plots in (**Fig. 24**) show that there is an overall agreement between the two distributions. At the leading edge on the suction side the difference in the two distributions is related to the fact that a fully turbulent profile is considered for the Calculated Results whereas in Xfoil a tripping position was established at $x_c/l_c = 0.05$.

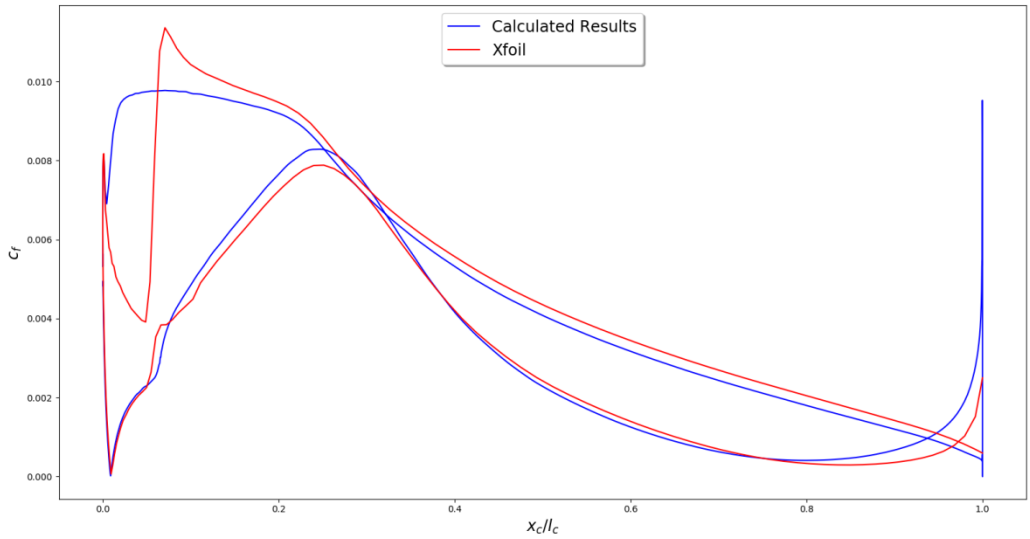

Fig. 24: *Skin friction coefficient distribution considering fully turbulent profile HL Airfoil*

In (**Fig. 25**) the two pressure coefficient distributions are presented. The same trend is captured for the two computations. Overall the values are also similar with the bigger differences occurring at the leading edge on the pressure side assuming values around six percent.

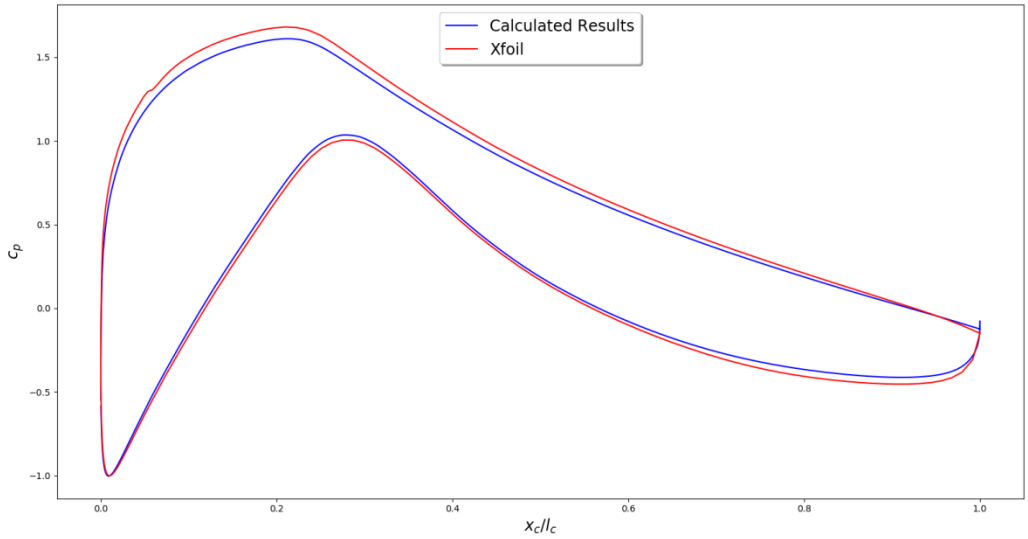

Fig. 25: *Pressure coefficient distribution considering fully turbulent profile HL Airfoil*

In (**Fig. 26**) the boundary layer thickness evolution along the suction side shows that around $x_c/l_c = 0.45$ the values computed in Calculated Results start to be smaller than the results obtained from Xfoil.

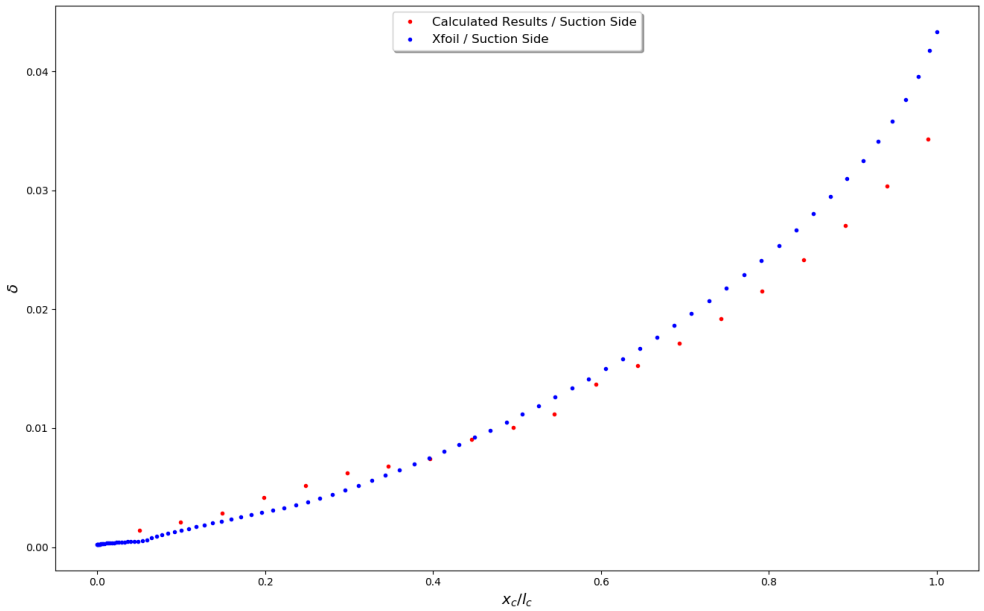

Fig. 26: *Boundary layer thickness evolution throughout the suction side of the HL Airfoil for a fully turbulent case*

In (**Fig. 27**) the displacement thickness for the Calculated Results tend to overestimate the value of the parameter compared to the Xfoil computations. Regarding the momentum thickness, the comparisons in (**Fig. 28**) revealed almost coincident results for the distribution of the parameter.

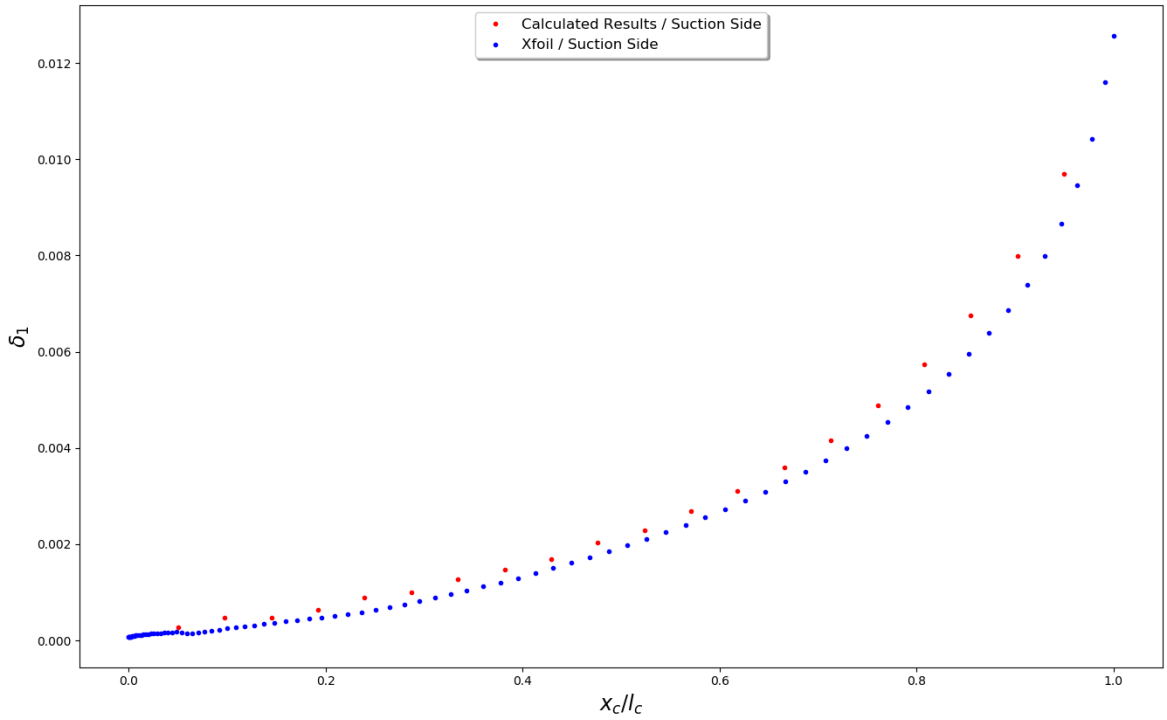

Fig. 27: *Displacement thickness evolution throughout the suction side of the HL Airfoil for a fully turbulent case*

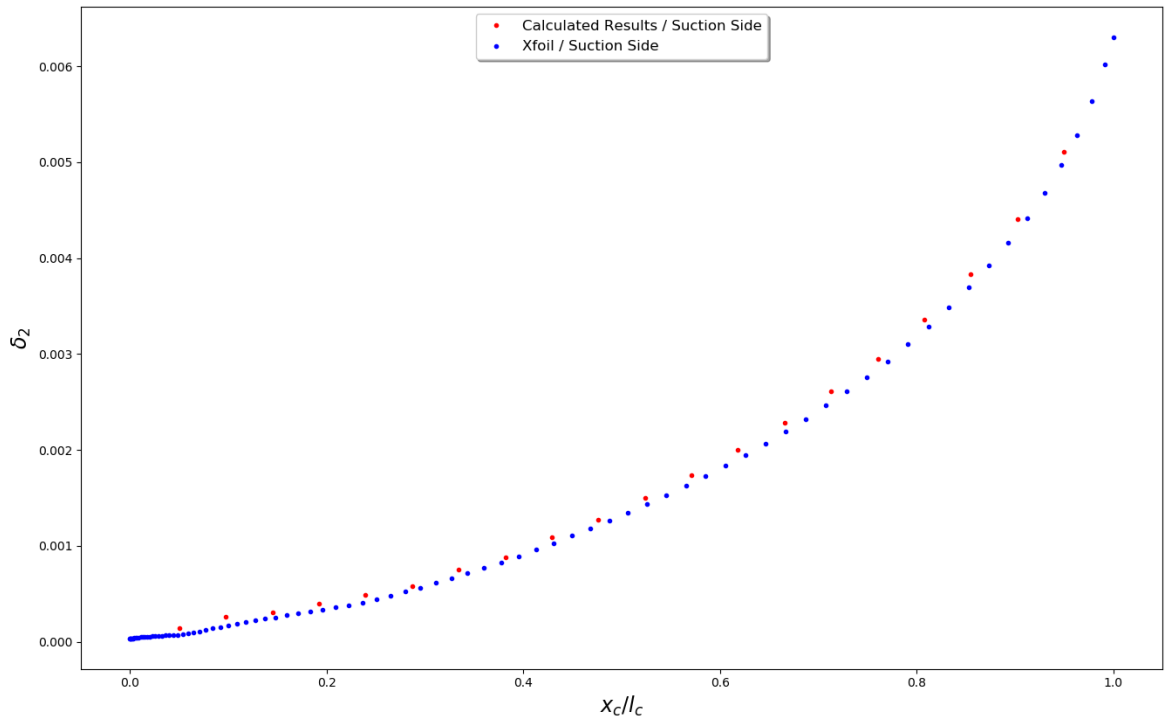

Fig. 28: *Momentum thickness evolution throughout the suction side of the HL Airfoil for a fully turbulent case*

Free Transition:

In this case, a natural transition velocity field along the surface of the airfoil is considered instead of a fully turbulent. The plots for the skin friction coefficient distributions are presented in (**Fig. 29**). In this case, Xfoil predicts for both sides of the airfoil an earlier start for the laminar-turbulent transition.

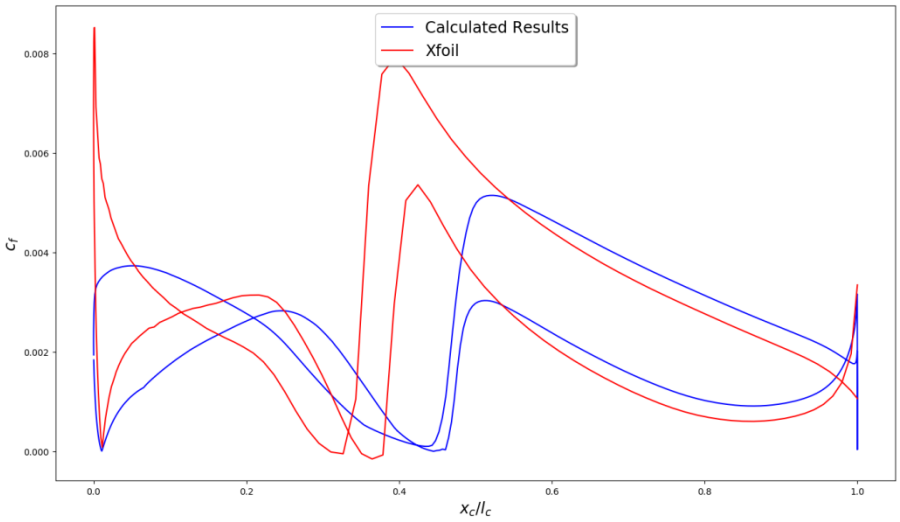

Fig. 29: *Skin friction coefficient distribution considering free transition HL Airfoil*

The plots in (**Fig. 30**) correspond to the pressure coefficient c_p and it is concluded from the figure that the two distributions are similar.

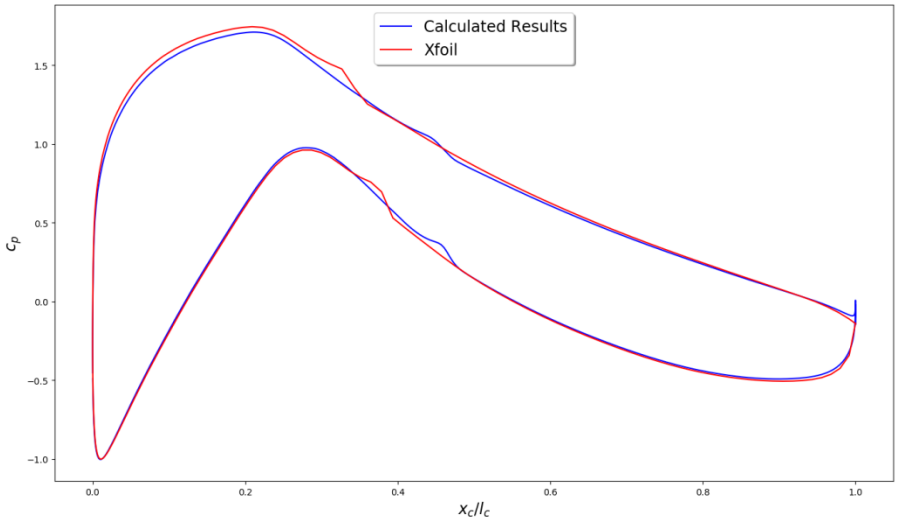

Fig. 30: *Pressure coefficient distribution considering free transition HL Airfoil*

In (**Fig. 31**) the representations for the boundary layer thickness reflect the differences in the c_f distributions since it is also noticeable that transition occurs at a different position for the two cases. The Calculated Results predict higher values for δ in the laminar stage whereas in the fully turbulent region these calculations tend to underestimate the parameters compared to Xfoil.

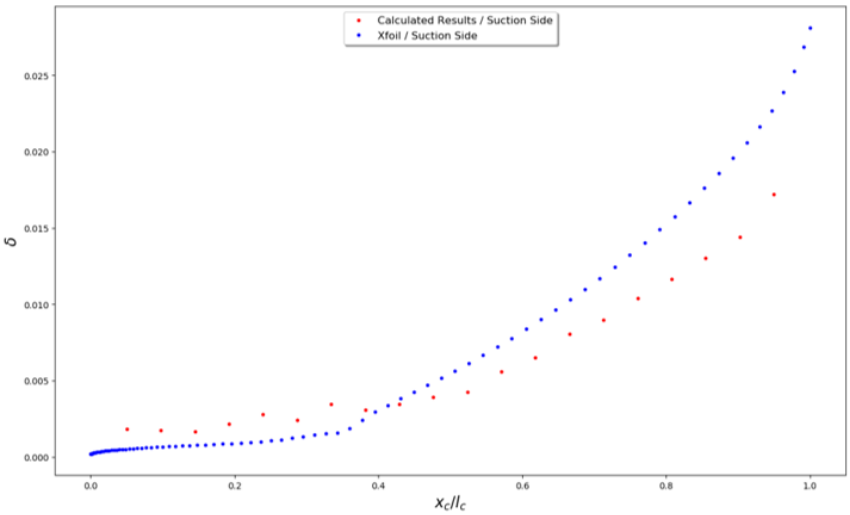

Fig. 31: *Boundary layer thickness evolution throughout the suction side of the HL Airfoil for a free transition case*

The plots in (**Fig. 32**) and (**Fig. 33**) represent the displacement and momentum thickness distributions, respectively. Also for these parameters, the Calculated Results predicted higher values than Xfoil in the laminar region and lower values for the fully turbulent region.

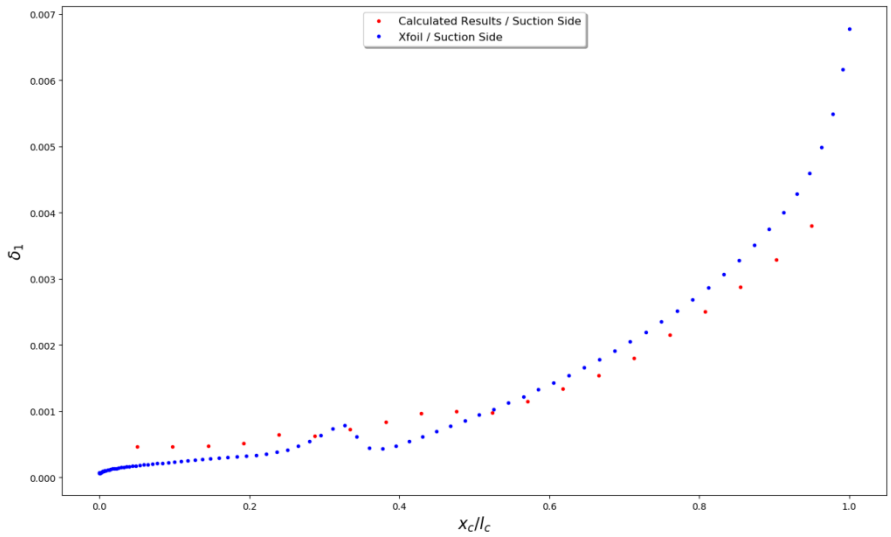

Fig. 32: *Displacement thickness evolution throughout the suction side of the HL Airfoil for a free transition case*

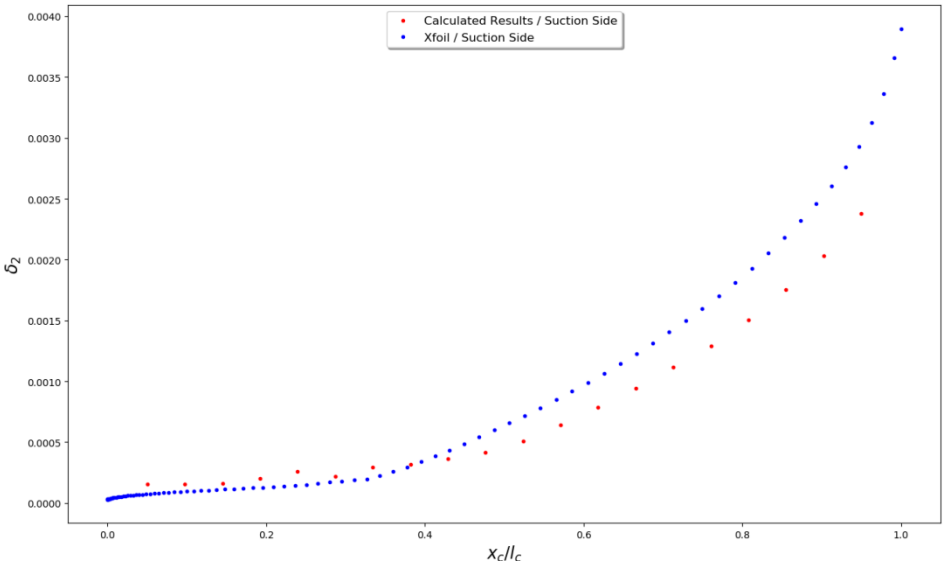

Fig. 33: *Momentum thickness evolution throughout the suction side of the HL Airfoil for a free transition case*

<u>LL Airfoil vs HL Airfoil:</u>

Different airfoil geometries translate in a different velocity field around the airfoils and, consequently, the aerodynamic performance of the airfoils is also distinct. The two airfoils considered here differ in shape and thickness resulting in different lift forces. The dissimilarities in the boundary layer parameters are analyzed. The momentum and displacement thickness at the trailing edge assume higher values for the LL Airfoil. Also, the difference when comparing the values of each parameters for the fully turbulent and free transition is bigger in the LL Airfoil.

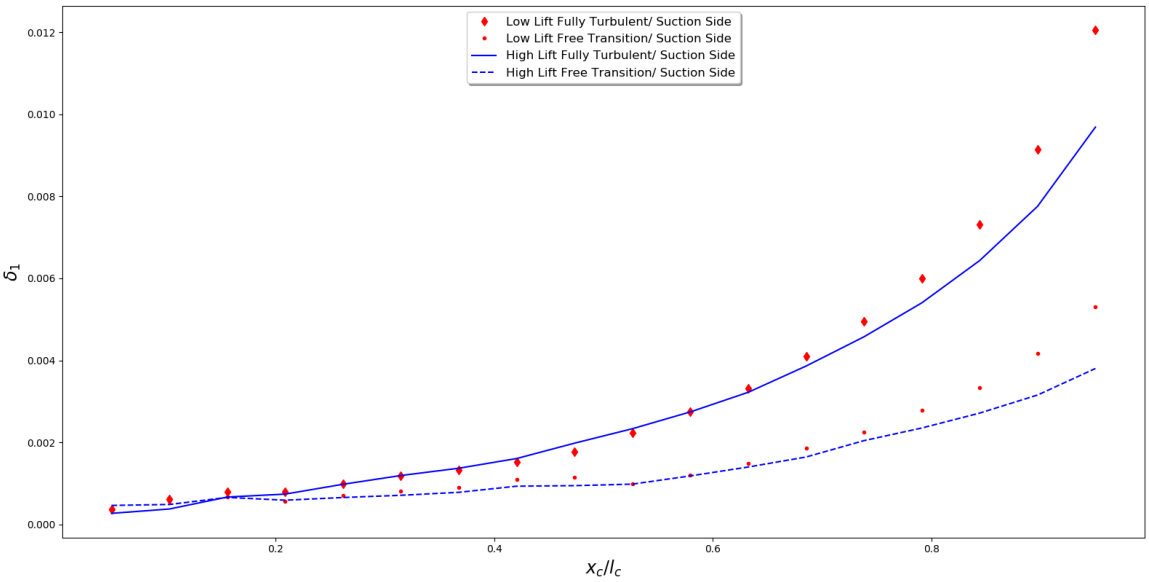

Fig. 34: *Displacement thickness evolution throughout the suction side of the LL and HL Airfoils*

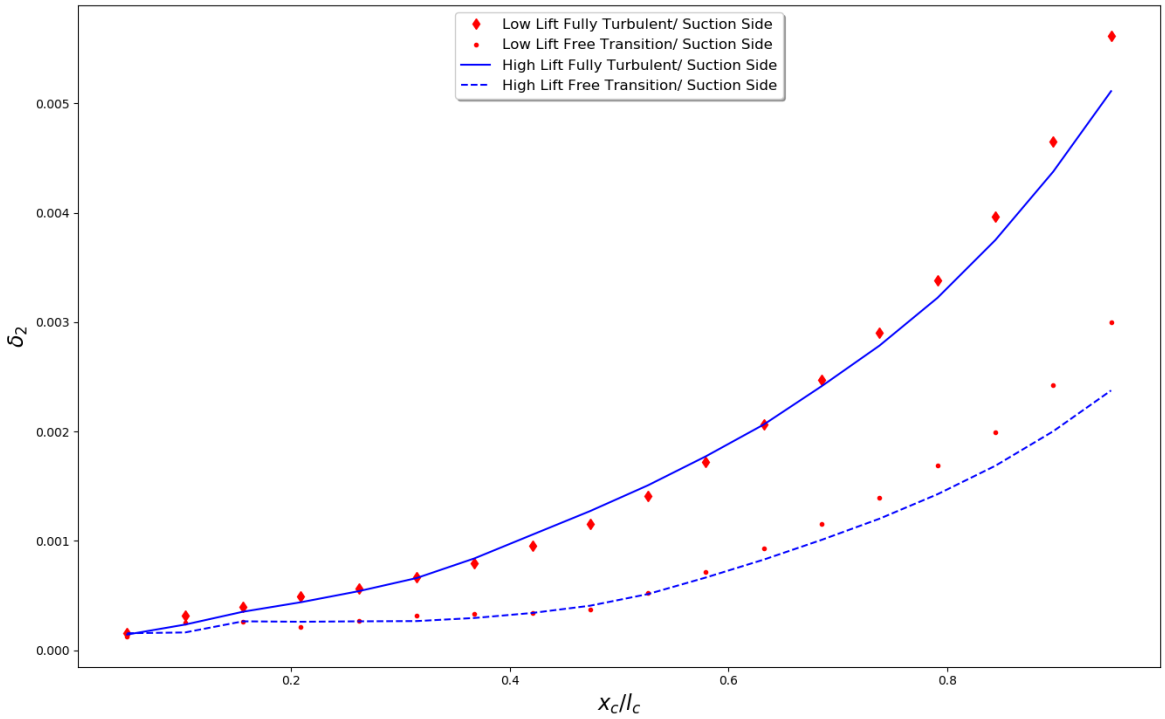

Fig. 35: *Momentum thickness evolution throughout the suction side of the LL and HL Airfoils*

3.2.5 CL Airfoil

To analyze how the mesh density used in the CFD simulations affects the computed results, two simulations using different mesh densities are considered.

The pressure coefficient distributions presented in (**Fig. 36**) and (**Fig. 37**) show that similar results are obtained for the situation with a denser mesh, least dense mesh, and xfoil. Although there are oscillations for the denser mesh case in (**Fig. 36**) the distribution follows the same trend.

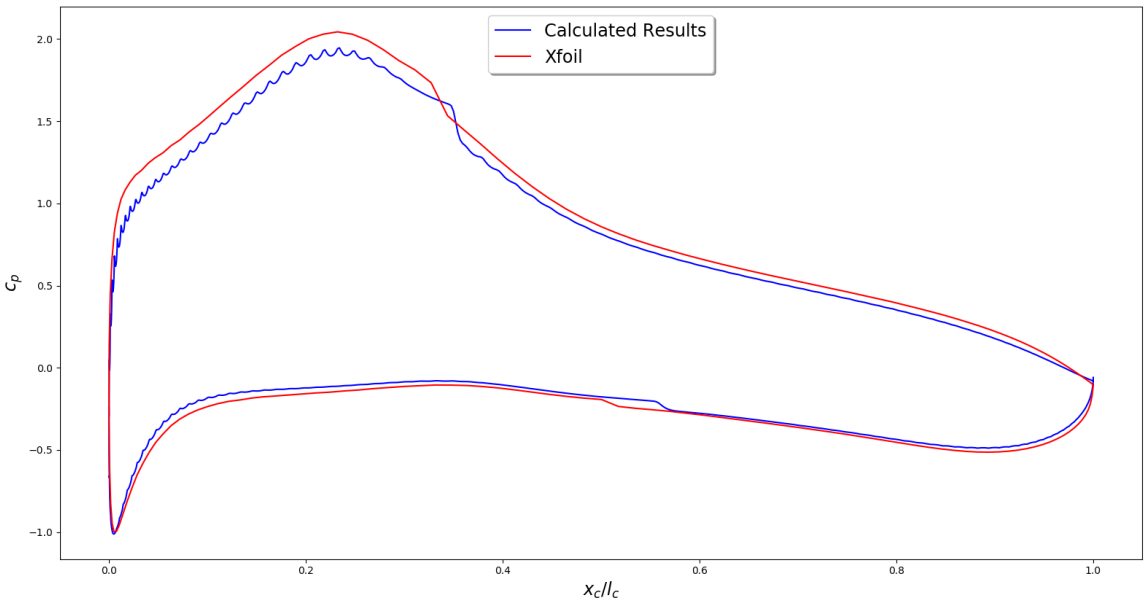

Fig. 36: *Cp distribution considering free transition for a CL Airfoil with a denser mesh*

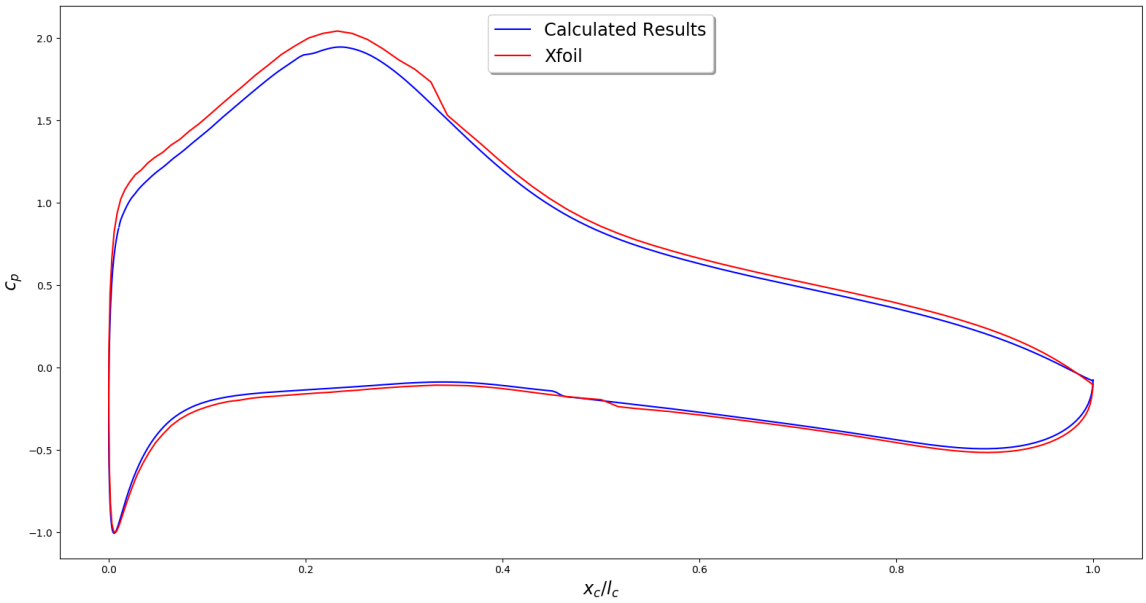

Fig. 37: *Cp distribution considering free transition for a CL Airfoil with a least denser mesh*

The skin friction coefficient plots are given for the denser and least dense mesh in (**Fig. 38**) and (**Fig. 39**), respectively. From (**Fig. 39**) it is concluded that in the situation with the least dense mesh the prediction of the laminar-turbulent transition was captured at different locations and for the denser mesh even though oscillations are present the distribution follows a similar trend compared to the Xfoil calculations.

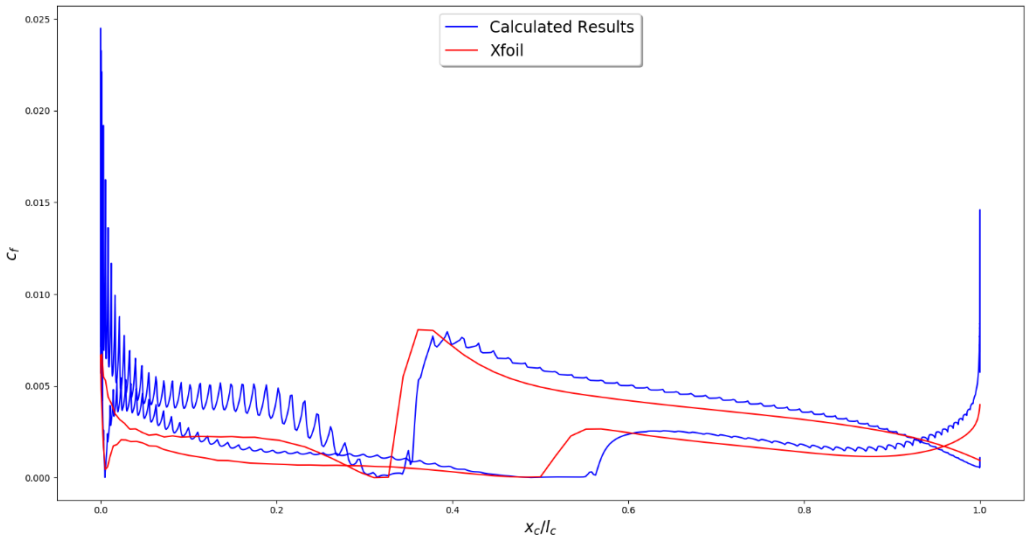

Fig. 38: *Cf distribution considering free transition for a CL Airfoil with a denser mesh*

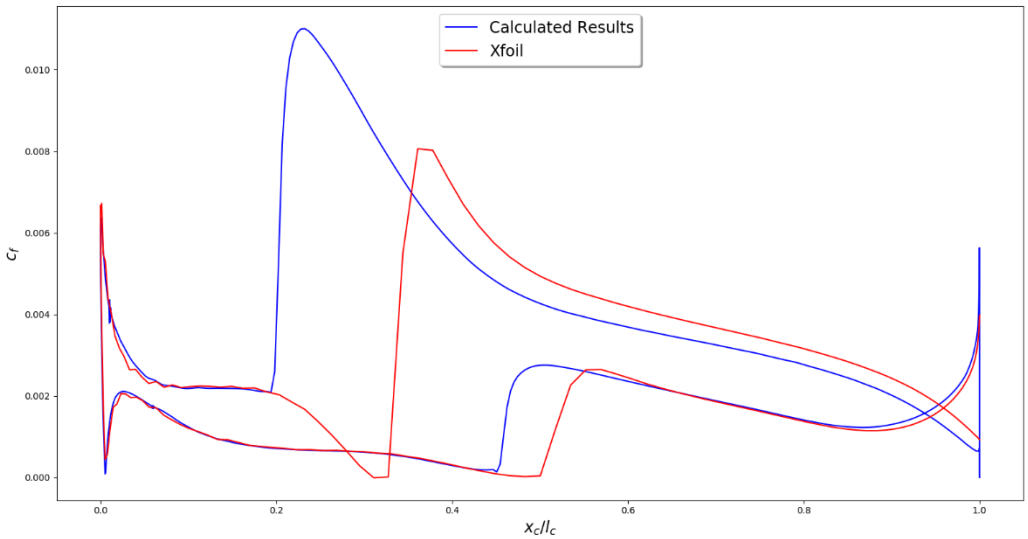

Fig. 39: *Cf distribution considering free transition for a CL Airfoil with a least denser mesh*

In the denser mesh computations an offset of 5.56 and 10.53 percent is obtained for the laminar-turbulent transition position on the suction and pressure side of the airfoil, respectively. For the least dense mesh the correspondent errors are of 37.5 and 12.5 percent.

Regarding the boundary layer thickness, the denser mesh results presented in (**Fig. 40**) captured the same trend as Xfoil but overestimated the values of δ throughout the airfoil with a maximum difference of nineteen percent. The results for the least dense mesh in (**Fig. 41**) when compared to the denser mesh show higher values for the difference with Xfoil because, as mentioned above, the laminar-turbulent transition occurs at different locations.

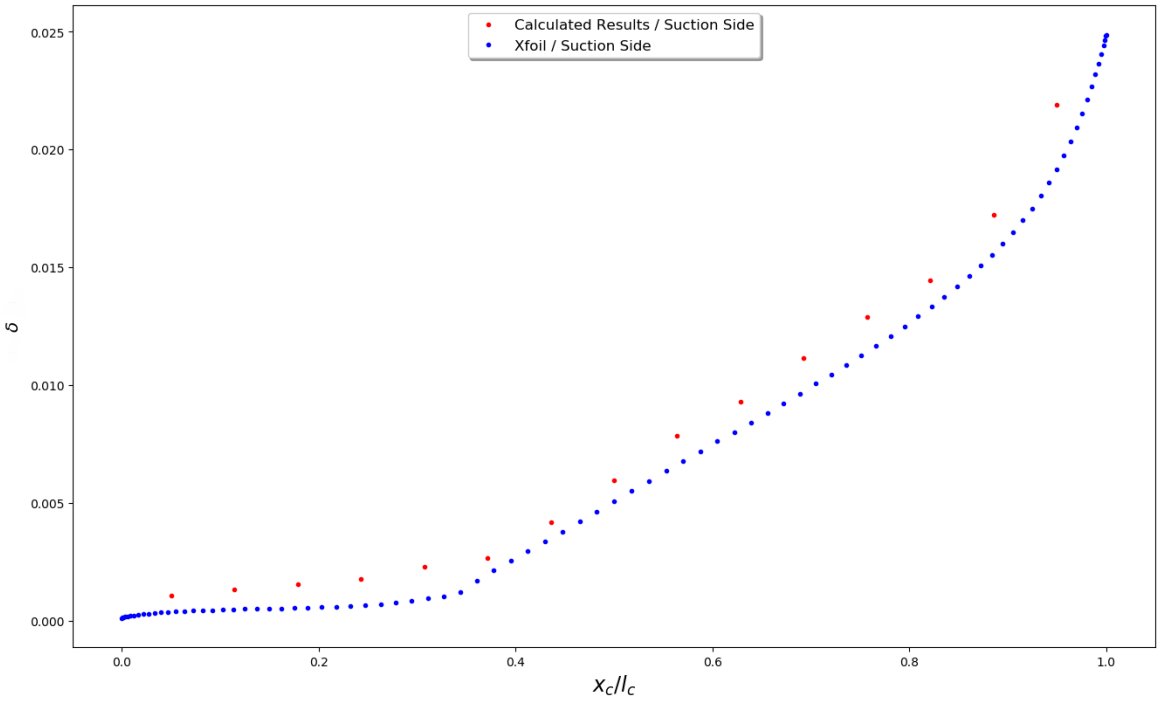

Fig. 40: *B.L. thickness evolution on the suction side considering free transition for a CL Airfoil with a denser mesh*

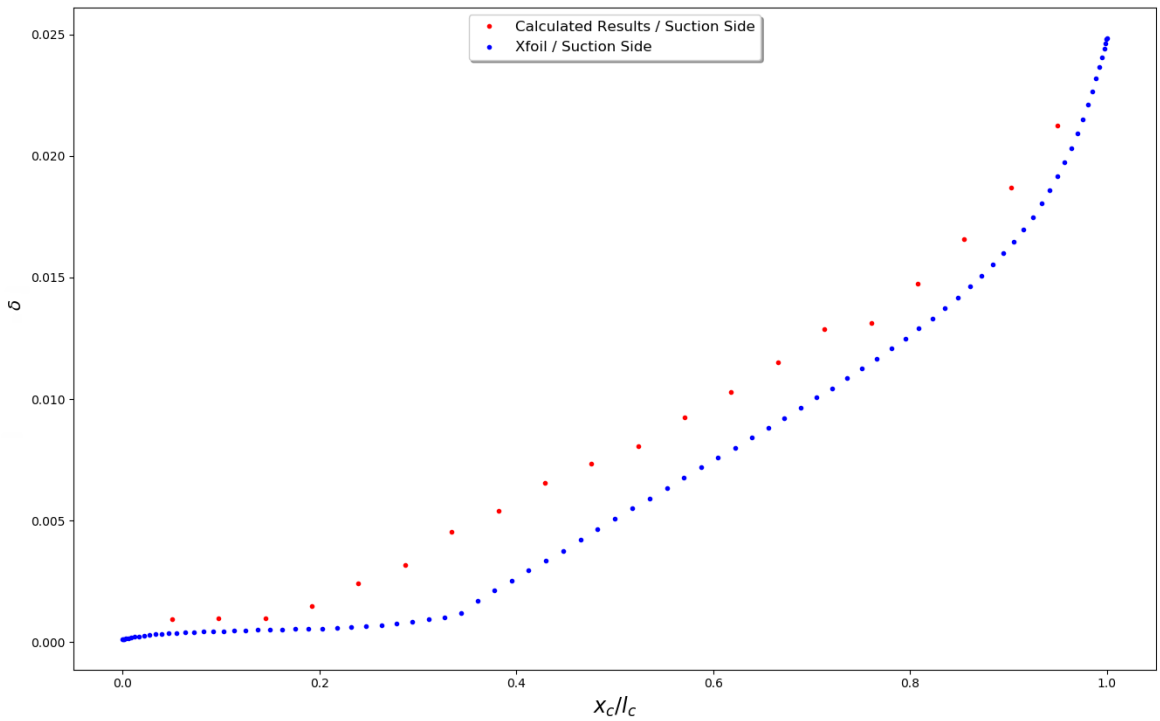

Fig. 41: *B.L. thickness evolution on the suction side considering free transition for a CL Airfoil with a least dense mesh*

The displacement thickness distribution plots are presented in (**Fig. 42**) and (**Fig. 43**) for the denser and least dense mesh, respectively. In this case, until transition the values computed with the denser mesh are closer to the Xfoil results. However, around $x_c/l_c = 0.6$ the two meshes obtained similar values.

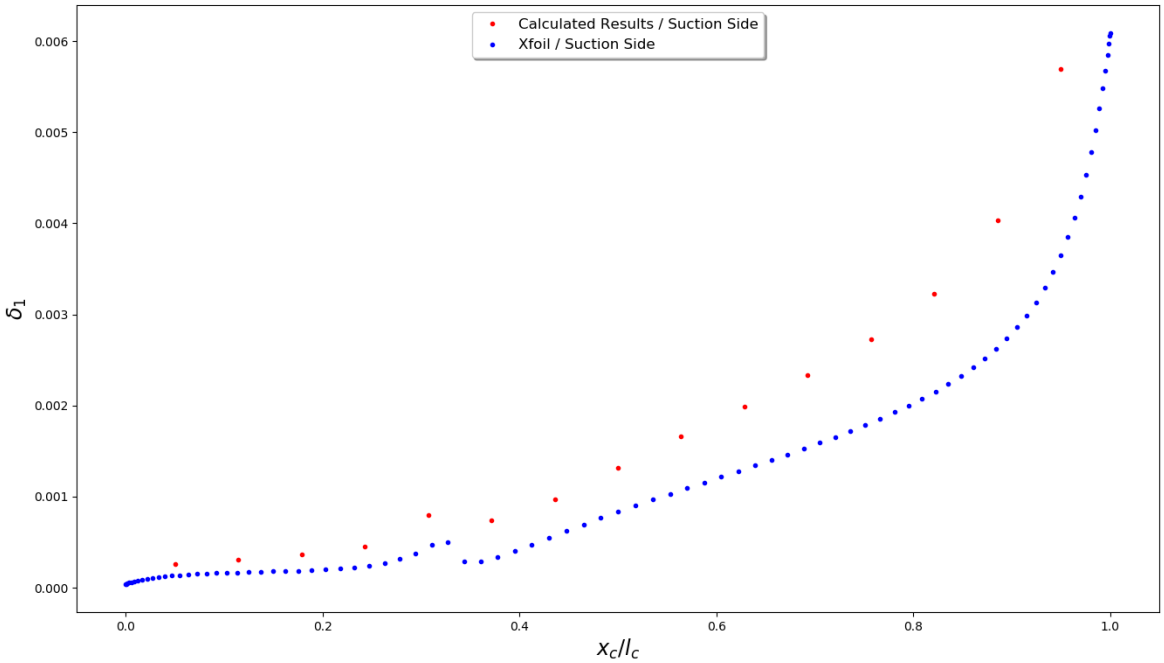

Fig. 42: *Disp. thickness evolution on the suction side considering free transition for a CL Airfoil with a denser mesh*

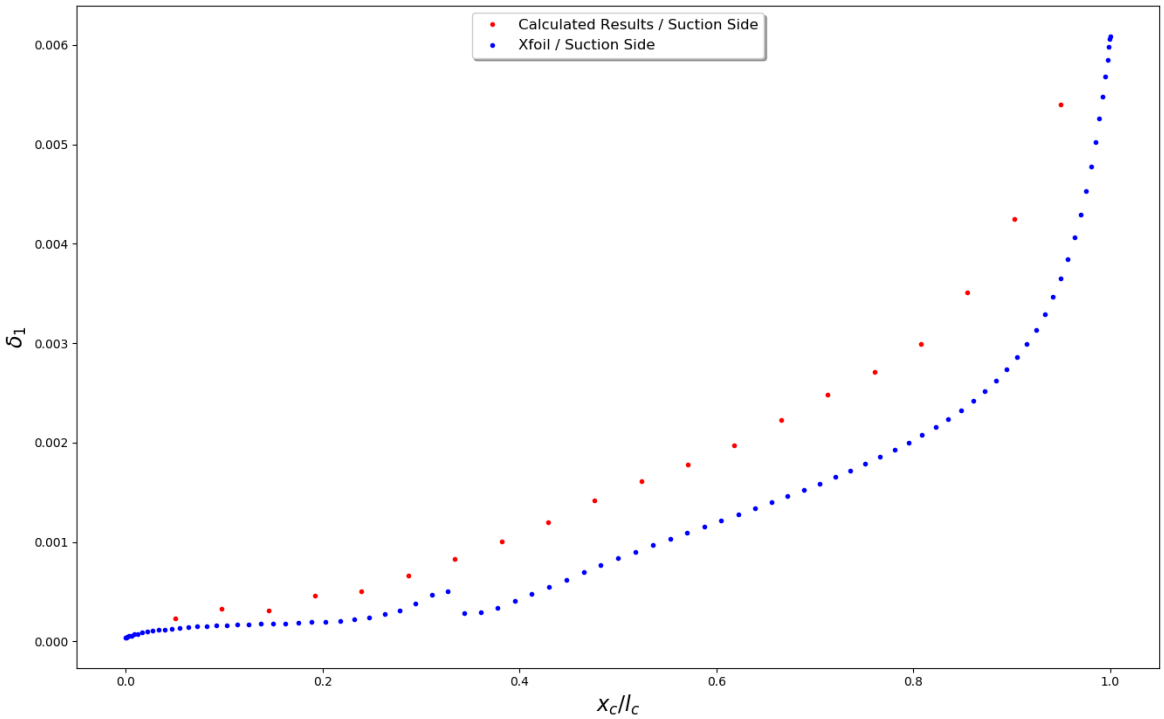

Fig. 43: *Disp. thickness evolution on the suction side considering free transition for a CL Airfoil with a least dense mesh*

The remarks made for the displacement thickness distributions apply for the momentum thickness distributions presented in (**Fig. 44**) and (**Fig. 45**).

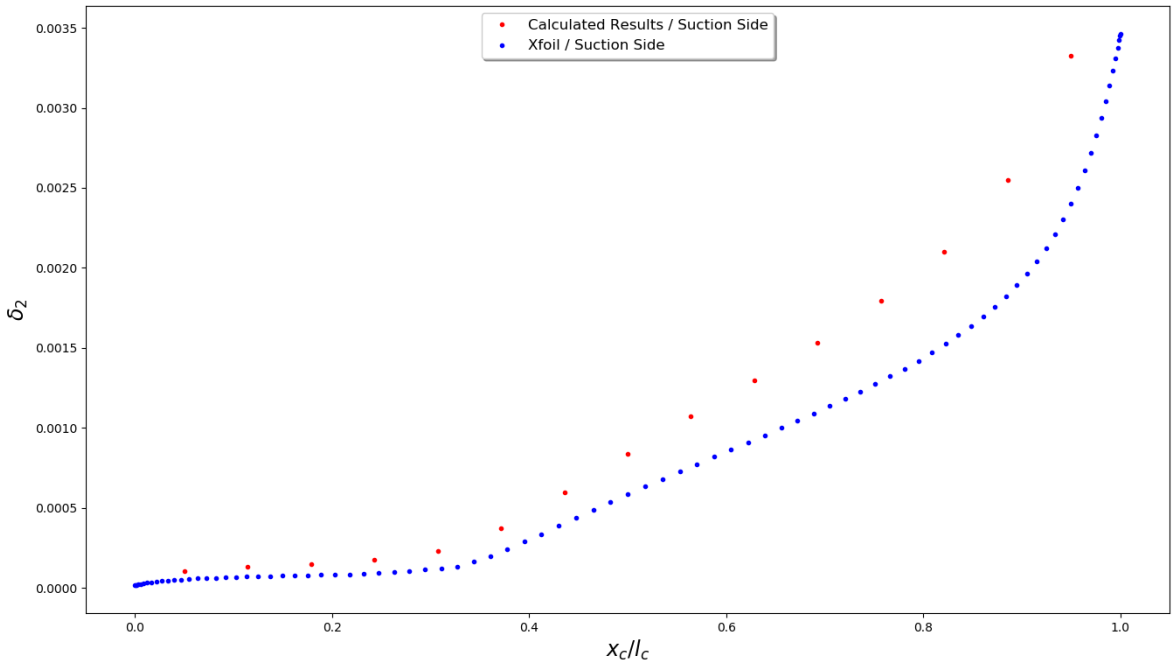

Fig. 44: *Mom. thickness evolution on the suction side considering free transition for a CL Airfoil with a denser mesh*

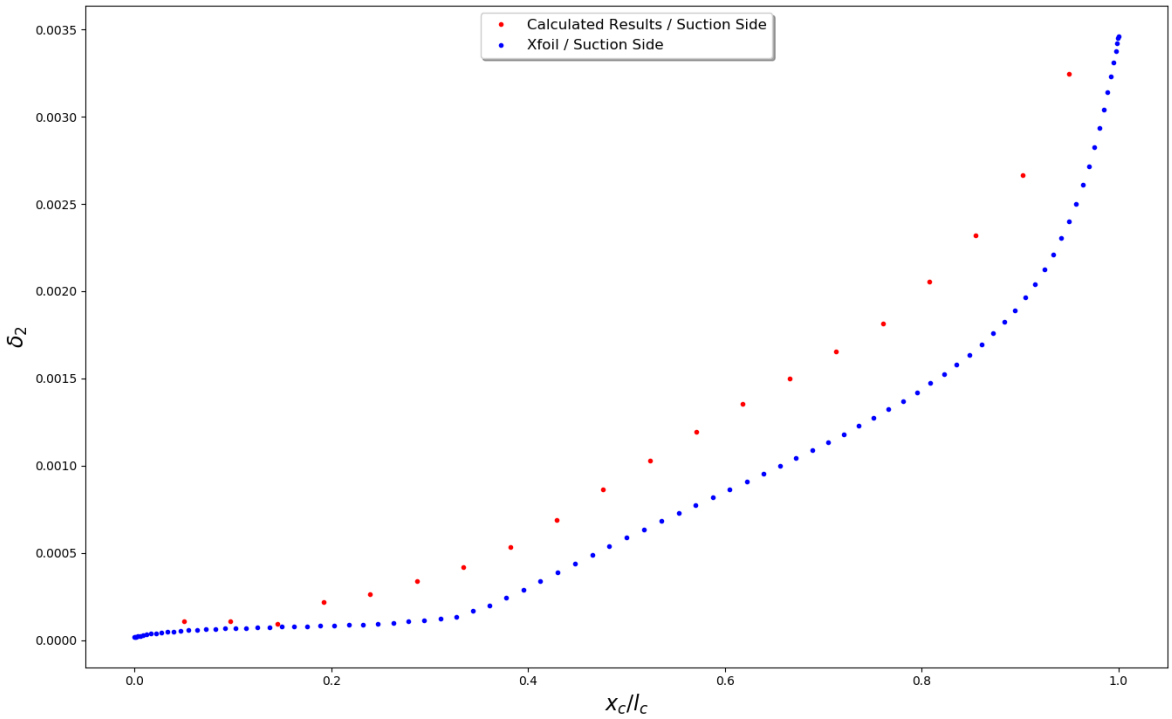

Fig. 45: *Mom. thickness evolution on the suction side considering free transition for a CL Airfoil with a least dense mesh*

4 Conclusions

The UL Airfoil case study is used to validate the post process tools. In this case, it is observed that the shape of the velocity profile at the trailing edge agrees with the profiles in [3]. The values of the integral boundary layer parameters are also similar, and it is concluded that the scripts are working correctly.

The use of wall functions to solve the boundary layer in the NACA 0012 simulations in the standard numerical simulation procedure resulted in an incorrect profile shape and, consequently, the calculated values for the integral boundary layer parameters are different from the values determined in the numerical simulations and experiments in [3]. For the Reynold's number and angles of attack considered in the simulation, increasing α results in the formation of a separation bubble, a phenomena that increases the complexity of the flow field around the airfoil; however, the error of the computed results relative to the values in [3] did not increase nor follow any particular trend.

The simulations for the LL and HL airfoils considered free transitional and fully turbulent situations. Congruent results are obtained in the different cases, this meaning that when a fully turbulent simulation is computed the value of the integral boundary layer parameters is higher. This difference accentuates the fact that when comparing results obtained from different simulations or experiments it is necessary to guarantee that the transition is captured identically. The calculated results displayed only a slight offset from the Xfoil computations.

The effects of mesh density are studied in the CL Airfoil simulations. The denser mesh results are in better agreement with Xfoil in terms of the integral boundary layer parameters and the position for the laminar-turbulent transition. Thus, based on this comparison, a mesh refinement should be adopted in the current standardized simulation procedure when dealing with the CL Airfoil.

The post process tools developed allow for an evaluation of the quality of a computational simulation using benchmark results and compute the integral boundary layer parameters. The study revealed that the scripts are working correctly, and that the in-house standardized numerical simulation procedure produced satisfactory results for all the airfoils tested except the NACA 0012.

References

[1] T. Brooks, S. Pope and M. Marcolini, "Airfoil Self-Noise and Prediction," NASA, Langley, 1989.

[2] AIAA, "2nd Workshop on Benchmark Problems for Airframe Noise Computations (BANC-II)," 2012.

[3] AIAA, "3rd Workshop on Benchmark Problems for Airframe Noise Computations (BANC-II)," 2014.

[4] H. Schlichting, Boundary Layer Theory, 7th Edition, vol. 36, McGraw Hill, pp. 74 - 82.

[5] Ansys Inc., "ANSYS CFX," [Online]. Available: https://www.ansys.com/products/fluids/ansys-cfx.

[6] M. Drela and H. Youngre, "XFOIL 6.9 User," Boston, 2001.

Appendix

Suzlon Energy Ltd. Background

Suzlon Energy Ltd., established in 1995, based from Pune, India, provides end to end solutions, in wind and solar energy, ranging from land acquisition to lifecycle asset management, and design to construction of associated facilities. Their clients include public electric utilities, independent power producers and corporate organizations in China, India, Europe, North America and Australia. Globally, Suzlon has over 17000 MW of wind power installations spread across 18 countries, with 11000 MW of capacity located in India. They have R&D offices in Germany, Denmark and Netherlands. The internship took place at one of Suzlon's R&D facility, located in Netherlands— Suzlon Blade Technology, Hengelo. It encompasses Aerodynamics & Loads, Materials and Structure, and Process Development Departments with dedicated R&D facilities for structural and material testing. The internship was conducted under the supervision of the Aerodynamics & Loads Department. This department is responsible for the design and optimization of wind turbine airfoils and blades.